HOST GALAXY PROPERTIES OF THE *Swift* BAT ULTRA HARD X-RAY SELECTED AGN

Michael Koss[1,2,3], Richard Mushotzky[1], Sylvain Veilleux[1], Lisa M. Winter[4,5], Wayne Baumgartner[2], Jack Tueller[2], Neil Gehrels[2], and Lynne Valencic[2]

Draft version July 6, 2011

ABSTRACT

We have assembled the largest sample of ultra hard X-ray selected (14-195 keV) AGN with host galaxy optical data to date, with 185 nearby (z<0.05), moderate luminosity AGN from the *Swift* BAT sample. The BAT AGN host galaxies have intermediate optical colors ($u − r$ and $g − r$) that are bluer than a comparison sample of inactive galaxies and optically selected AGN from the Sloan Digital Sky Survey (SDSS) which are chosen to have the same stellar mass. Based on morphological classifications from the RC3 and the Galaxy Zoo, the bluer colors of BAT AGN are mainly due to a higher fraction of mergers and massive spirals than in the comparison samples. BAT AGN in massive galaxies (log $M_* > 10.5$) have a 5 to 10 times higher rate of spiral morphologies than in SDSS AGN or inactive galaxies. We also see enhanced far-IR emission in BAT AGN suggestive of higher levels of star formation compared to the comparison samples. BAT AGN are preferentially found in the most massive host galaxies with high concentration indexes indicative of large bulge-to-disk ratios and large supermassive black holes. The narrow-line (NL) BAT AGN have similar intrinsic luminosities as the SDSS NL Seyferts based on measurements of [O III] λ5007. There is also a correlation between the stellar mass and X-ray emission. The BAT AGN in mergers have bluer colors and greater ultra hard X-ray emission compared to the BAT sample as whole. In agreement with the Unified Model of AGN, and the relatively unbiased nature of the BAT sources, the host galaxy colors and morphologies are independent of measures of obscuration such as X-ray column density or Seyfert type. The high fraction of massive spiral galaxies and galaxy mergers in BAT AGN suggest that host galaxy morphology is related to the activation and fueling of local AGN.

Subject headings: galaxies: active — X-rays: interactions — X-rays: galaxies

1. INTRODUCTION

Most galaxies with bulges harbor a supermassive black hole in their center (Magorrian et al. 1998), yet only a small fraction exhibit the powerful radiative or kinetic output associated with an active galactic nucleus (AGN). While it is well established that matter falling onto the supermassive black hole is emitted as energy, the source of this material remains highly controversial. To understand what activates and continues to fuel AGN, we must better characterize the conditions of the host galaxies in which they are found. What environmental factors trigger these black holes to begin emitting so much energy and what continues to fuel this process?

Numerical simulations suggest that quasars ($L_{bol} > 10^{45}$ erg s^{-1}) are the end product of mergers between gas-rich disk galaxies, and that supermassive black hole accretion heats the interstellar material and quenches star formation leading to passive elliptical galaxies (di Matteo et al. 2005). Alternatively, other simulations suggest sources other than mergers may fuel lower luminosity AGN, such as gas streaming down galactic bars or steady cold gas streams (Mulchaey & Regan 1997; Hopkins & Hernquist

2006; Dekel et al. 2009).

A number of observational studies have provided interesting yet contradictory results about the relationship between the host galaxy and the AGN. A study of the host galaxies of X-ray selected AGN from the Extended Chandra Deep Field-South found that AGN are in the most luminous galaxies, with intermediate optical colors, and bulge dominated morphologies (Silverman et al. 2008). Another study of narrow emission line (NL) AGN in the Sloan Digital Sky Survey (SDSS) found the hosts were predominantly massive early-type galaxies and the most luminous AGN galaxies had significant star formation (Kauffmann et al. 2003). An additional survey of the SDSS NL AGN host galaxies found, compared to a sample of nearby inactive galaxies, most AGN occur along the red sequence (Westoby et al. 2007). Even though these studies draw their conclusions from large optical surveys or soft X-ray surveys, their results may be biased by missing an important population of obscured AGN.

A less biased survey of AGN must account for absorption of light by gas and dust. In addition, the survey must distinguish between host galaxy emission primarily from stars and emission from AGN. Historically, an inability to account for these factors provided different results depending upon the wavelength used for observation. Initially, AGN were selected by radio techniques (Heckman 1980) or optically using broad and strong emission lines, a luminous point-like nucleus, or irregular galaxy color (Weedman 1977). The presence of broad optical emission lines was used to separate Seyfert 1 galax-

mkoss@astro.umd.edu

[1] Astronomy Department, University of Maryland, College Park, MD, USA
[2] Astrophysics Science Division, NASA Goddard Space Flight Center, Greenbelt, MD, USA
[3] Institute for Astronomy, University of Hawaii, Honolulu, HI, USA
[4] Center for Astrophysics and Space Astronomy, University of Colorado, Boulder, CO, USA
[5] Hubble Fellow

ies with broad permitted and narrow forbidden lines and Seyfert 2 galaxies with only narrow permitted and forbidden line emission. In the unified model (Antonucci 1993) both broad line Seyfert 1 galaxies and obscured Seyfert 2 galaxies are intrinsically the same, with the differences being the viewing of the central engine. Surveys of AGN taken in the optical, UV, and soft X-rays (< 2 keV) miss an important population of obscured narrow line AGN only visible in the ultra hard X-ray and mid-IR wavelengths (Mushotzky 2004; Koss et al. 2011). While the mid-IR wavelength is less obscured, this wavelength range is problematic because of confusion with emission from star formation, sensitivity to the amount of obscuring material, and the lack of a unique way to select AGN from other luminous IR galaxies (Stern et al. 2005; Hickox et al. 2009). Therefore, the ultra hard X-ray, >15 keV range offers an important new way to select AGN for a less biased survey.

The BAT survey is an all sky survey in the ultra hard X-ray range that has identified 461 objects of which 262 are AGN (Tueller et al. 2010). The BAT instrument is a large field of view (1.4 steradian) coded aperture imaging instrument. Because of the large position error of BAT ($\approx 2'$) higher angular resolution X-ray data for every source from Swift-XRT or archival data have been obtained allowing associations with 97% of BAT sources. This sample is particularly powerful since the BAT is sensitive in the 14–195 keV band and at obscuring columns of $>10^{24}$ cm^{-2} where only high-energy X-ray emission (tens of keV) can pass through the obscuring material. It is therefore sensitive to heavily obscured objects where even hard X-ray surveys ($L_{2-10\,keV}$) are severely reduced in sensitivity. At 22 months[6], the BAT survey has a sensitivity of approximately 2.2×10^{-11} erg cm^{-2} s^{-1}. With this sensitivity, the BAT survey is about 10 times more sensitive than the previous all-sky ultra hard X-ray survey, HEAO 1 (Levine et al. 1984). About 15%, or 30 of the AGN, have never before been detected as AGN at other wavelengths.

While AGN host galaxy studies using X-ray surveys typically probe objects at moderate redshift (out to z$\approx$1), more nearby (z$<$0.05) AGN offer the best opportunity to study the host in detail since high spatial resolution data are easily obtainable. The majority of the BAT AGN are nearby with a median redshift of 0.03. Thus, a study of the BAT AGN sample provides an excellent opportunity to answer the controversial question of AGN fueling and its relationship to the host galaxy.

The BAT AGN sample have already provided several interesting results about their host galaxies. One study found that BAT AGN show a merger rate of 24% compared to only 1% in normal galaxies (Koss et al. 2010). A study of the morphologies based on NED classifications and DSS imaging found a majority to be in spirals or peculiars (Winter et al. 2009). Other studies found that BAT AGN have been shown to have additional reddening of the narrow line region not accounted for in optical studies and be misclassified as star forming or composite regions (Winter et al. 2010; Meléndez et al. 2008). In the case of host galaxy colors, two studies using <20 BAT AGN reached different conclusions: Schawinski et al. (2009) found that the AGN tend to

be in intermediate or red galaxies and possibly suppress star formation, while Vasudevan et al. (2009) found BAT AGN in blue, starforming galaxies. This contradiction highlights a major problem in current AGN host galaxy studies: the paucity of large, uniform samples with high quality data. To make progress on this issue, we have assembled the largest sample of ultra hard X-ray selected AGN with host galaxy optical data to date, with 185 AGN in total. The BAT AGN and comparison samples are discussed in §2; data reduction and analysis in §3 with additional discussion of removal of AGN light in appendix §A, the comparison sample in §B, and selection effects in appendix §C; the results in §4; and the summary and discussion in §5.

2. SAMPLES

2.1. *BAT AGN Sample*

We selected our sample to focus on Seyfert AGN in the BAT sample which contribute the large majority, 87% of the total sample, and 99% of the nearby, z$<$0.05 sample. We use the classifications of Tueller et al. (2010) to exclude beamed sources such as blazars. We also restrict the sample to nearby AGN (z$<$0.05) which includes 80% of the BAT sample. These AGN can be further classified on the basis of broad or narrow emission lines. We define NL AGN as having H$\alpha <$2000 km/sec using spectroscopic data from Winter et al. (2010), Ho et al. (1997), and the SDSS. For those BAT galaxies without spectra, we use the SDSS galaxy class separator or available data from NED to separate NL and broad-line objects. The BAT sample has 50% (93/185) NL and 50% (92/185) broad-line sources. In addition to including the entire range from unobscured to highly obscured, the AGN have moderate luminosities (log $L_{2-10\,keV} \approx 43$), and therefore accretion rates, typical of the local universe.

By imposing an upper redshift limit (z$<$0.05) to the sample, we focus on galaxies that are close enough to have good spatial resolution (700 pc) from ground-based optical imaging. We further restrict our survey to Northern declinations ($>$-25°). We also exclude six nearby galaxies with bright foreground Galactic stars where photometry is difficult and three nearby bright galaxies with saturated pixels. This survey covers 125 nearby AGN or 50% of the entire BAT AGN sample from the 22 month survey. We also included an additional 60 AGN galaxies detected in the 58 month BAT sample catalog (Baumgartner et al. 2010, submitted) with X-ray followup with the *Swift* XRT telescope that showed a coincident source to the 14–195 keV BAT source in the 2–10 keV band.

The optical imaging data for these galaxies include 17 nights at the Kitt Peak 2.1m telescope in the *ugriz* SDSS bands (Table 1) and data from the SDSS (Table 2). The final Kitt Peak and SDSS sample includes a total of 185 galaxies, 79 BAT AGN host galaxies observed at Kitt Peak, 92 from the SDSS, and 14 galaxies observed by both the SDSS and at Kitt Peak.

2.2. *Comparison Samples*

To better understand the host galaxy properties of BAT AGN, we used a comparison sample of inactive galaxies and a sample of emission line selected AGN from the SDSS. We will henceforth refer to the three samples

as the *BAT AGN, inactive galaxies*, and *SDSS AGN*, respectively.

The inactive galaxies were selected from the SDSS to have high quality photometry and similar redshifts as the BAT AGN. We selected all non-QSO galaxies from the SDSS DR7 with spectra and imaging data with redshift confidence, z_{conf}>0.9 and a redshift interval similar to the BAT AGN (0.01<z<0.07). We chose this slightly higher redshift interval because many of the SDSS galaxies with z<0.01 are too bright to be targeted in spectroscopy. We also removed NL Seyfert or LINER AGN from this sample using emission line diagnostics (Kewley et al. 2006) and the Garching catalog of reduced spectra of narrow line AGN (Kauffmann et al. 2003). Galaxies totaled 68,275. We will refer to this sample as the *inactive galaxy sample.*

Finally, we used a sample of emission line selected AGN in the SDSS for comparison, which we refer to as the *SDSS AGN*. Winter et al. (2010) found that the majority (75%) of a sample of 64 BAT AGNs were Seyferts. Only 3/64 (<5%) of BAT AGN were classified as LINERS, so we excluded this type of AGN from the comparison sample. We chose narrow-line AGN since the nucleus is invisible in the optical band and thus does not have to be modeled to determine the host galaxy properties. We therefore chose a sample of all type 2 Seyferts in the SDSS DR7 with 0.01<z<0.07. We used 1282 Seyferts in this redshift range.

To ensure that the BAT AGN were not more intrinsically luminous than the SDSS AGN sample of Seyferts, we compared the [O III] of the BAT AGN with available spectra to the SDSS AGN (Fig. 1). When measuring [O III], we used the narrow Balmer line ratio (Hα/Hβ) to correct for extinction assuming an intrinsic ratio of 3.1 and the Cardelli et al. (1989) reddening curve. For reference we also included LINERS in the SDSS. For the BAT AGN we used spectroscopic data from Winter et al. (2010), Ho et al. (1997), and the Garching Catalog of SDSS spectra Kauffmann et al. (2003). We find that the BAT AGN have similar [O III] luminosities as the SDSS NL Seyferts, suggesting that they also have similar intrinsic luminosities (although there may still be differences, see §5). We find a similar relation when only including sources with SDSS spectroscopy and excluding spectroscopic data from Winter et al. (2010) and Ho et al. (1997).

3. DATA ACQUISITION, REDUCTION, AND ANALYSIS

Throughout this work, we adopt the following cosmological parameters to determine distances: Ω_m= 0.27, Ω_Λ= 0.73, and H_0 = 71 km s^{-1} Mpc^{-1}. For galaxies with z<0.01, we use the mean value of redshift independent measurements from NASA Extragalactic Database (NED) when available. Unless otherwise noted, error bars correspond to 1σ standard deviation of the sample.

3.1. *Data Acquisition*

The Kitt Peak sample was obtained in February 2008 and November 2008 using the t1ka, t2ka, and t2kb CCDs on the 2.1m telescope. A random sample of *gri* tricolor images that have been flux calibrated using the procedure of Lupton et al. (2004) are shown in Fig. 2. Each galaxy was imaged so that a high signal-to-noise ratio
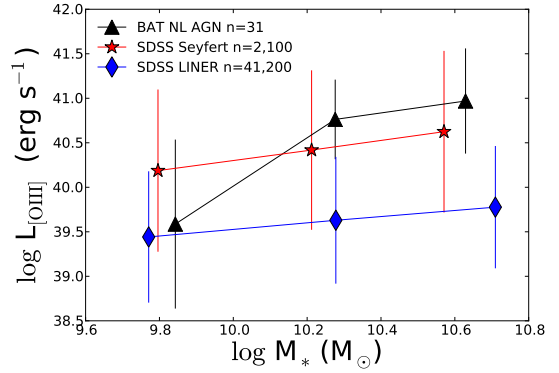
Figure 1. Average [O III] luminosities for the NL AGN in the BAT sample compared to the SDSS sample of narrow-line Seyferts and LINERS. The error bars indicate standard deviations in each bin. We find that the distributions of [O III] from the NL BAT AGN and NL SDSS Seyferts used in this study are from the same parent population (P(K-S)=82%). The [O III] luminosity is a measure of AGN power and suggests the NL BAT AGN have similar AGN power as SDSS NL Seyferts.

Figure 2. Random sample of 18 *gri* composite images of galaxies in the BAT AGN sample taken at Kitt Peak. An arcsinh stretch was used with flux scaled by magnitudes (Lupton et al. 2004).

could be achieved to capture faint features and low surface brightness emission with 12 minutes in *u* and 6 minutes in *griz*. The *u* images were obtained at twice the imaging time because of the higher sky brightness and lower signal-to-noise ratio in this band. Limiting magnitudes and observing conditions can be found in Table 3.

3.2. *Initial Calibration*

The initial imaging analysis involved calibration of zero point magnitudes, coadding SDSS plates for larger galaxies, and removing extraneous sources (e.g. foreground stars, other galaxies). For calibration of the Kitt Peak data, we used the primary standard star network of 158 stars used by the SDSS for calibration (Smith et al. 2002). A calibration star was imaged before and after each galaxy at similar airmass. Extinction coefficients were determined using standard stars on a nightly basis. Standard IRAF routines were used to remove bias, dark current, and CCD non-linearity. Galactic extinction corrections were made based on data from *IRAS* and *COBE/DIRBE* (Schlegel et al. 1998). For 8 SDSS galaxies extending across multiple SDSS plates, the MONTAGE software was used to reproject the images, rectify background and coadd plates. WCSTools was used to register Kitt Peak images from USNO stars (Mink

1996). Nearby foreground stars and galaxies were identified using segmentation maps produced by SExtractor (Bertin & Arnouts 1996). The segmentation map identified object pixels using a threshold of 3σ and a minimum of 5 pixels in $griz$. In the u band, the detection threshold was set to 1σ to ensure that faint star forming regions were detected. The segmentation map was visually compared to three color gri images to ensure proper star and galaxy separation. Stellar or foreground galaxy objects were masked with the IRAF FIXPIX routine.

3.3. *Host Galaxy Photometry*

The residual host galaxy colors were measured after removing the AGN light contribution using GALFIT. To ensure that the AGN emission was properly removed we performed simulations of AGN galaxies to test GALFIT and also checked the subtraction for BAT AGN (see Appendix §A for a discussion). A modified form of the Petrosian system, the same as is used in the SDSS automated pipeline, was used for photometry (Blanton et al. 2001) for both the SDSS and Kitt Peak observed BAT AGN galaxies. The Petrosian aperture is determined to be large enough to enclose almost all of the flux for typical galaxy profiles, but small enough that the sky noise is not significant. For consistency, the Petrosian aperture is determined from the r band and applied to the other bands. A galaxy with a bright stellar nucleus, such as a broad-line Seyfert galaxy, can have a Petrosian radius set by the nucleus alone; in this case, the Petrosian flux misses most of the extended light. Therefore the Petrosian radius in the r band was determined after the AGN model from GALFIT was subtracted. We then used the software KCORRECT (Blanton & Roweis 2007) with the $ugriz$ photometry to calculate the stellar masses. This code uses the stellar population models of Bruzual & Charlot (2003) and photoionization models of Kewley et al. (2001). We used the same software to calculate the stellar mass for the inactive galaxy and SDSS AGN control samples.

We also made a comparison of the overlapping galaxy data from the SDSS and Kitt Peak to ensure there were no systematic differences in photometry. In some cases, the automated SDSS pipeline's photometry shreds bright galaxies into many smaller galaxies which leads to incorrect photometry estimates for bright, nearby galaxies (see Appendix §B). For cases where shredding wasn't a problem, the colors of overlapping galaxies observed at Kitt Peak and in the SDSS showed good agreement in $griz$ with mean color differences less than 0.02 mag and sample standard deviation less than 0.05 mag. The u band is more uncertain with mean $(u - g)= 0.05 \pm 0.16$ mag brighter for the Kitt Peak measurements. This difference is expected because the u band measurements in the SDSS have a lower signal-to-noise ratio and also suffer from a red leak[7].

There were also ten nearby galaxies or 5% of the sample with pixel saturation in the SDSS images because of a bright nucleus. For these galaxies we masked the saturated pixels and fit the remaining image with a point source (PS) and floating Sérsic Index. We then used the model fit to recover the saturated pixels. We restricted using this method to those galaxies with saturation in a

single imaging band with <25 pixels saturated. This excluded three very nearby galaxies ($z<0.005$; NGC 1068, NGC 4151, NGC 3998) with saturated pixels in multiple filters from the study. For five images of nearby galaxies taken at Kitt Peak, the estimated Petrosian radius extended beyond the edge of the CCD. In these cases we used the maximum part of the image available to determine the photometry. In addition, 16 galaxies or 9% had very low signal-to-noise ratio measurements in the u band and were not included in the photometry.

We have also provided a detailed discussion of the selection effects in the X-ray selected BAT sample of AGN, and the optically selected SDSS AGN and inactive galaxies (see Appendix §B and C). These selection effects are also included to enable comparison with AGN surveys at other wavelengths and for comparison with high-z studies.

4. RESULTS

4.1. *Colors, Internal Extinction, and FIR emission*

Since host galaxy color traces star formation, a comparison of BAT AGN host galaxy colors to a sample of inactive galaxies should show whether the AGN is linked to enhanced or suppressed star formation. A full listing of the photometry measurements of the different samples can be found in Table 4. A plot of $g-r$ and $u-r$ for BAT AGN, inactive galaxies, and optical AGN can be found in Fig. 3. We find that the BAT AGN are bluer in both $g-r$ and $u - r$ than the sample of inactive galaxies and SDSS AGN in all but the lowest stellar mass bin (Table 5). A Kolmogorov-Smirnov (K-S) test indicates a $<1\%$ probability that the distribution of host galaxy colors for the BAT AGN are from the same parent distribution as the inactive galaxies or SDSS AGN.

Host galaxy colors can be reddened in galaxies with high inclinations and large amounts of dust, so we measure whether these corrections change our result that the BAT AGN tend to be bluer than inactive galaxies or SDSS AGN. Because of the relative uncertainty in these measurements, we do not apply individual reddening corrections on any plots, but estimate how reddening corrections effect the average colors of the samples. In Fig. 4, we show tricolor images of the 6 reddest and bluest BAT AGN host galaxies in $g - r$. The predominance of face-on spirals in the bluest sample and edge-on spirals in the reddest sample indicates the need for reddening correction based on inclination. Masters et al. (2010) studied internal extinction of galaxies identified as spirals in Galaxy Zoo and provided corrections based on the measured inclination from the SDSS photometry. For the three samples, we find that the average extinction for spiral galaxies is similar (0.04 ± 0.03 in $g - r$), but because of the higher number of spirals in the BAT AGN sample compared to SDSS AGN or SDSS inactive galaxies (see §4.2), there is a larger extinction correction for the BAT AGN sample.

There are galaxies that have high levels of star formation, but are reddened in the optical wavelengths because of the presence of dust. For example, in the BAT AGN sample, the reddest galaxy in $g - r$ is NGC 6240, a luminous infrared galaxy (LIRG) in a major merger, which shows a large amount of star formation in the far-IR. This indicates that dust can play a significant role

---

[7] http://www.sdss.org/dr7/algorithms/fluxcal.html
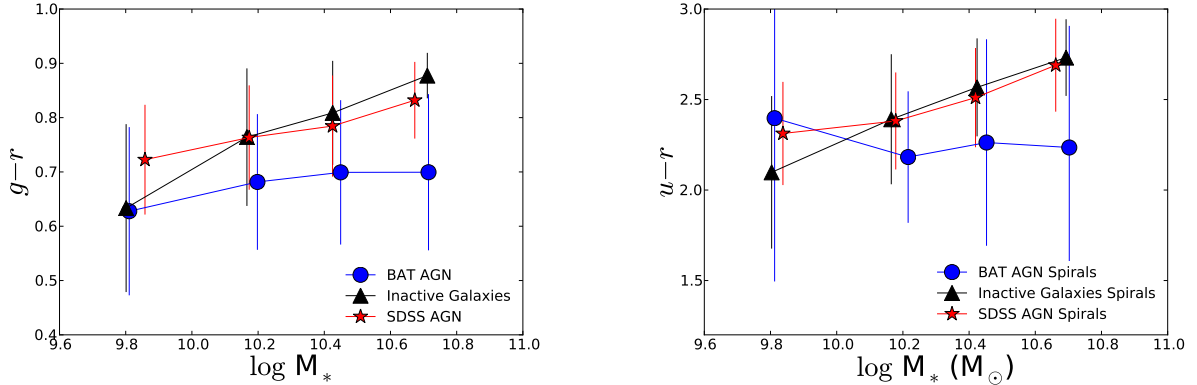
Figure 3. Plot of average Petrosian $g - r$ and $u - r$ for BAT AGN, inactive galaxies, and SDSS AGN. We find that the BAT AGN have bluer average colors than inactive galaxies or SDSS AGN in all but the lowest stellar mass bin. The error bars indicate standard deviations in each bin.
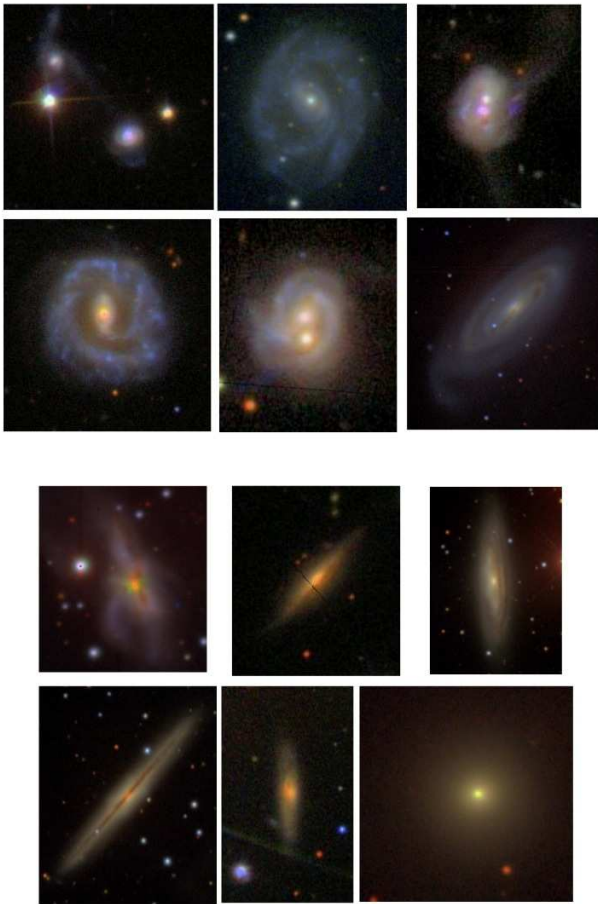
Figure 4. *Upper*: Tricolor images of six bluest BAT AGN host galaxies in $g - r$. We find that these BAT AGN are predominantly in mergers and face on spirals. *Lower*: Tricolor images of six reddest BAT AGN host galaxies in $g - r$. We find that 4/6 of these BAT AGN are in edge-on spirals that are reddened by internal extinction. The predominance of face on spirals in the bluest galaxies and edge-on spirals in the reddest galaxies indicate the need for a reddening correction based on inclination.

in reddening the optical light and hiding increased levels of star formation. Therefore, we estimate the total dust extinction (A_V) for each galaxy by fitting the host $ugriz$ SEDs using FAST (Kriek et al. 2009) with single-burst stellar population models. We use stellar templates from Bruzual & Charlot (2003) with the Chabrier (2003) initial mass function and solar metallicity. We fit a Calzetti et al. (2000) dust extinction reddening law ($A_V = 0$–3). We assume that $R_V = 3.1$, and therefore E(B-V)=A_V/3.1. We find that the reddening determined using fits to the optical SED of BAT AGN (0.34 ± 0.26 in $g - r$) are on average larger than for comparable inactive galaxies (0.20 ± 0.14) or SDSS AGN (0.21 ± 0.13). Therefore, we do not find evidence that the bluer measured colors of BAT AGN, compared with those of inactive galaxies and SDSS AGN, can be explained as smaller dust reddening. In fact, reddening corrections make the BAT AGN even bluer than comparable SDSS AGN or inactive galaxies. We also find that the reddening corrections for host galaxy inclination are on average much smaller than dust reddening (0.04 ± 0.03 vs. 0.34 ± 0.26 in $g - r$).

The far-IR provides an additional tracer of star formation that is less sensitive to reddening than shorter wavelengths. The 90 μm emission is a useful tracer of strong bursts of recent star formation and is less affected by AGN emission (Netzer et al. 2007; Mullaney et al. 2011). We first looked at the rate of detection in *AKARI* in each of the samples in the same redshift range ($0.01 < z < 0.05$). In this redshift range, $54 \pm 5\%$ (86/185) of BAT AGN are detected by *AKARI* at 90 μm, compared to only $4 \pm 1\%$ of SDSS AGN, and $5 \pm 1\%$ of inactive galaxies. The error bars represent 1σ Poisson statistics.

To ensure this difference was not an effect of the differences in the distribution of stellar mass and redshift of the samples, we matched each BAT AGN to one inactive galaxy and one SDSS AGN based on redshift and stellar mass. We find a similar percentage for both inactive galaxies $7 \pm 3\%$ (11/158) and SDSS AGN $3 \pm 2\%$ (5/158) detected by *AKARI*. The error bars represent 1σ Poisson statistics.

While there is a possibility of AGN contamination in the 90 μm emission, the similar levels of *AKARI* detections for the inactive galaxies and SDSS AGN indicate that this level of contamination is limited. In addition, the AGN contamination to the FIR should be similar for BAT and SDSS AGN since the [O III] luminosities are similar and [O III] is an indicator of bolometric luminosity. All of these results indicate that the BAT AGN are more luminous at 90 μm, which suggests enhanced star

formation among BAT AGN when compared to SDSS AGN and inactive galaxies.

4.2. *Host Galaxy Morphology*

We investigated galaxy morphology to find which environments are most conducive to hosting an AGN and how ultra hard X-ray selected AGN are different than the SDSS AGN or inactive galaxies. A full listing of the morphological measurements can be found in Table 6. While we have limited our results to NL AGN because of the difficulty of subtracting the light distribution to make morphological measurements (Pierce et al. 2010), we provide morphological measurements of broadline AGN after AGN light subtraction with GALFIT in Table 6.

The first measure we compared was concentration. To enable comparison with the SDSS, the concentration index is defined as the ratio of the radii containing 90 and 50 per cent of the Petrosian r-band galaxy light $C = R_{90}/R_{50}$. A galaxy with a steep concentration profile, such as an elliptical, will show a relatively large value for the C, while galaxies with a more shallow light profile, such as spiral and irregular galaxies, will have a lower C. In addition, the concentration index is strongly correlated with the galaxy's bulge to total luminosity ratio as well as the supermassive black hole mass. A plot of concentration vs. stellar mass is shown in Fig. 5 for BAT AGN compared to inactive galaxies and SDSS AGN. We find that at low stellar mass (log $M_* < 10$), BAT AGN tend to have higher concentrations than inactive galaxies or SDSS AGN indicative of stronger bulges or a larger fraction of elliptical galaxies. However, as shown below, the BAT AGN sample has a very low elliptical galaxy fraction.

While C measurements are useful, they have been shown to be more closely related to luminosity than morphology (Gavazzi et al. 2000). Since the human eye has consistently proven better than computational techniques at identifying faint spiral structure in images (Lintott et al. 2008), we used a catalog of visual classifications from the Galaxy Zoo project DR1 (Lintott et al. 2008). Before morphological classification, we matched each NL BAT AGN to one inactive galaxy and one SDSS AGN by redshift and stellar mass. We then used the visual classifications of morphology to divide host galaxies into elliptical, spiral, intermediate, and peculiar/merger. Each galaxy had on average 37 independent classifications for a total of over 15,000 classifications for the 3 samples. Elliptical or spiral galaxies were defined as galaxies in which on average >80% people selected this type. We define the peculiar/merger category following Patton & Atfield (2008) and Koss et al. (2010) by requiring a projected separation of <30 kpc and a radial velocity differences of less than 500 km/s between the sample galaxy and its possible companion. The remainder of galaxies we classify as intermediate.

A comparison between the Galaxy Zoo classifications of the samples can be found in Fig. 6. We find that BAT AGN are more likely to be found in spiral morphologies at a rate (41%) roughly twice that of inactive galaxies (22%) or SDSS AGN (21%). We also find fewer BAT AGN in elliptical or intermediate types. We confirm that BAT AGN are more likely to be found in merging systems consistent with the result of Koss et al. (2010). We see
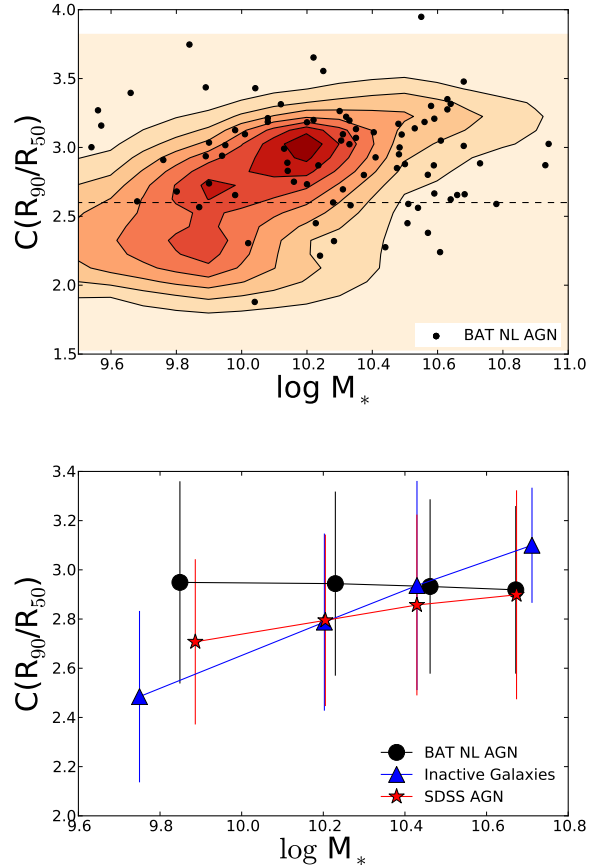
Figure 5. *Upper Panel*: Plot of concentration vs. stellar mass with contours showing inactive galaxies and points for the BAT AGN. The contour levels are plotted on a linear scale with each level representing 10% of the data (6875 inactive galaxies). A dashed line is shown at C=2.6 at the separation between early and late types. *Lower Panel*: Plot of average concentration index by stellar mass. We find that at low stellar mass (log $M_* < 10$), BAT AGN tend to have higher concentrations than inactive galaxies or SDSS AGN. The error bars indicate standard deviations in each bin.

no statistically significant differences in the morphologies of inactive galaxies or SDSS AGN.

In addition, we looked at the Hubble Types of the BAT AGN sample compared to the Third Reference Catalog of Bright Galaxies (RC3) to confirm our results with Galaxy Zoo. We used all galaxies in the RC3 in the same redshift range as the BAT AGN. The RC3 is composed of bright galaxies with optical B mag<15.5 and size larger than 1′. This restriction excludes many faint galaxies or about 98% of the SDSS sample in the same redshift range. The BAT AGN sample has slightly higher optical luminosities than the RC3 (mean $M_B = -20.33\pm0.82$ vs. $M_B = -20.03\pm1.03$) and is at similar distances (mean z=0.025±0.01 vs. z=0.019±0.01 for the RC3). We find more BAT AGN in early type Sa-Sb spirals (40%) compared to the RC3 catalog (26%). We see fewer BAT AGN in ellipticals (3%) compared the RC3 catalog (16%). The larger number of spiral morphologies in the BAT AGN sample is consistent with our analysis of morphologies using Galaxy Zoo.

Since spiral galaxies tend to be found in less massive systems than elliptical galaxies, we examined the rela-
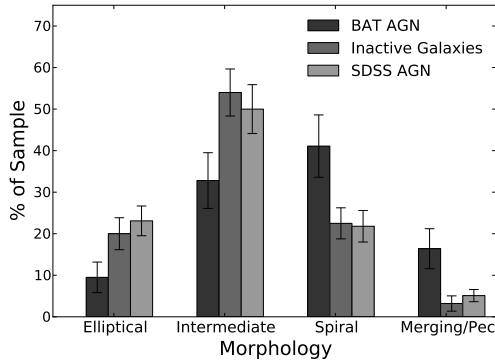
Figure 6. Histogram of morphologies from the BAT AGN, inactive galaxies, and SDSS AGN. The morphologies were taken from measurements in the Galaxy Zoo DR1. The error bars represent 1σ Poisson statistics. We find a higher incidence of spirals in the BAT AGN sample and less ellipticals and intermediates. We also find more merging/peculiar types in the BAT AGN sample.
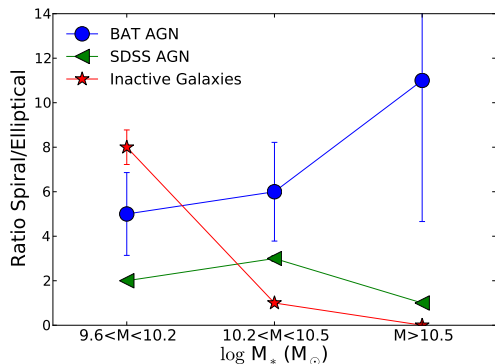
Figure 7. Ratio of the number of spiral to elliptical galaxy morphologies as a function of stellar mass (M_*). Galaxy morphologies are taken from Galaxy Zoo. The error bars represent 1σ Poisson statistics. We find that the BAT AGN have a much larger number of massive spirals (log M_* >10.5) and very few ellipticals compared to inactive galaxies or optical AGN.

tionship between morphology and stellar mass. For the BAT AGN in spirals, we find a higher average stellar mass (log M_*=10.34±0.27) than in ellipticals and intermediates (log M_*=10.07±0.42). A K-S test indicates a <4% the populations are the same. This finding is in agreement with Schawinski et al. (2010) that found that optical AGN in elliptical systems tend to be in less massive systems. We further investigated the predominance of massive spirals amongst BAT AGN by plotting the ratio of the number of spiral to elliptical galaxies by stellar mass (Fig. 7). For massive systems (log M_* >10.5), we find that BAT AGN are found in spirals at a rate that is 5 to 10 times higher than optical AGN or inactive galaxies.

We also examined the galaxy inclination. A study of SDSS galaxies by Maller et al. (2009) found that elliptical galaxies rarely have small axis ratios, and galaxies with b/a<0.55 are 90% disk galaxies. Therefore the axis ratio can be a reliable quantitative tracer of morphology. To enable comparison with the SDSS catalog, we used the galaxy axis ratio in the g band (b/a). The axis ratio (b/a) is determined from the major and minor axes
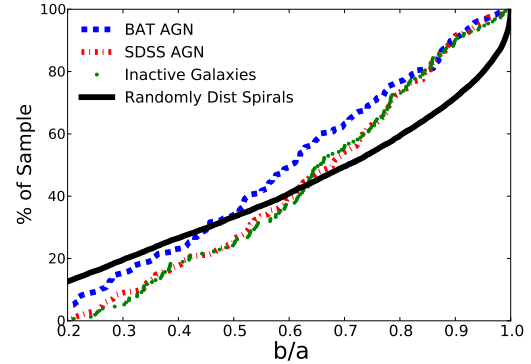

Figure 8. Cumulative distribution of galaxy axis ratios in the r band (b/a) for the NL BAT AGN, inactive galaxies, and SDSS AGN. The axis ratio (b/a) is determined from the major and minor axes derived from SDSS isophotal photometry. Randomly distributed spirals with a $\cos\theta$ distribution of axis ratios is shown for reference. We find that more NL BAT AGN have b/a<0.55 than inactive galaxies and SDSS AGN. This limit is where Maller et al. (2009) found almost 90% disk-like systems, and is consistent with increased incidence of spirals in NL BAT AGN compared to inactive galaxies and SDSS AGN.

derived from SDSS isophotal photometry. A plot of axis ratios of the samples can be found in Fig. 8. For the axis ratios, we find a larger percentage of NL BAT AGN have b/a<0.55 which is where Maller et al. (2009) found almost 90% disk-like systems. This result is consistent with the increased incidence of spirals found by Galaxy Zoo for the BAT AGN. We find no difference between the axis ratios of the inactive galaxies or SDSS AGN.

Previous studies have suggested that optical emission line classification of Seyfert galaxies may be missing a population of edge on galaxies (Kirhakos & Steiner 1990; Simcoe et al. 1997). Since the NL BAT AGN are more likely to be in disk galaxies which have lower axis ratios, we separated the samples by morphology in Galaxy Zoo and then did a comparison of axis ratio. In this case we do not see any statistically significant difference in axis ratios between NL BAT AGN spirals compared to spirals in inactive galaxies or SDSS AGN.

Finally, the SDSS catalog provides independent measurements of the fraction of early type galaxies from the photometry and spectroscopy. The SDSS spectroscopic parameter eClass classifies the spectral type of the galaxy using the principal component analysis technique, and the photometric parameter fracDev$_r$ measures the fraction of galaxy light that is fitted by a de Vaucouleurs law. Following Bernardi et al. (2003) we define as early type galaxies those objects with eClass<0 from spectroscopy and fracDev$_r$ > 0.8 from photometry. In this comparison we only use NL BAT AGN with spectroscopy in the SDSS (185). We find a statistically smaller number of NL BAT AGN in early type galaxies (39%±8), compared to inactive galaxies (61%±6) or SDSS AGN (56%±6). The error bars represent 1σ Poisson statistics. These results are consistent with a spectroscopic study of 64 BAT AGN which found that the majority of NL BAT AGN have spectra consistent with late type galaxies based on measurements of the stellar absorption indices (Winter et al. 2010). The percentage of BAT AGN galaxies classified as early type galaxies (39%±8) using SDSS spectroscopy is significantly larger than that based
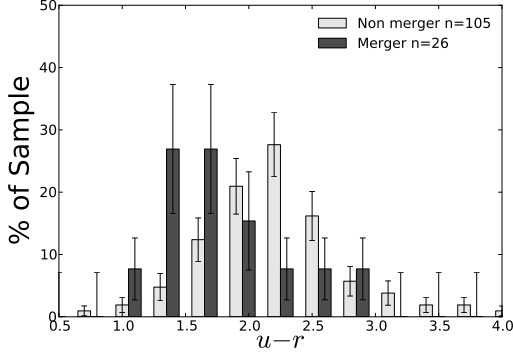
Figure 9. Histogram of $u-r$ colors of BAT AGN in major mergers vs. BAT AGN that are not in major mergers. The error bars represent 1σ Poisson statistics. The merging galaxies show a bluer distribution of colors than non-mergers. We find a similar trend in the $g-r$ colors.
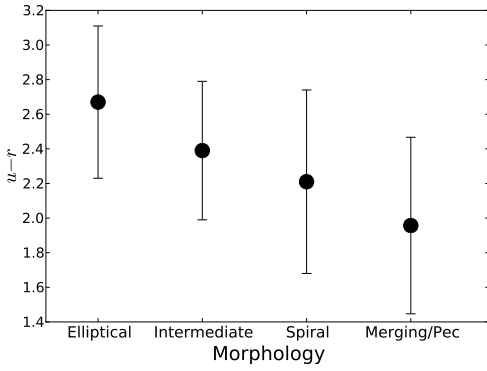
Figure 10. Average $u-r$ color for different morphologies of BAT AGN. The error bars indicate standard deviations in color for each morphology. Galaxy morphologies were taken from Galaxy Zoo. We find spiral and merger morphologies are on average bluer than elliptical or intermediate morphologies. We find a similar trend in the $g-r$ colors.

on morphological measurements from the RC3 or galaxy zoo (3% and 10% respectively). This is likely because the SDSS spectroscopy uses a $3''$ aperture and is measuring only the central bulge portion of the galaxy.

4.3. *Colors, Morphology, and Ultra Hard X-ray Emission*

Since we found BAT AGN host galaxies have a greater number of merger and spiral morphologies, an additional question is how this is related to host galaxy colors. To test this we used a sample of BAT AGN in the process of mergers (Koss et al. 2010) and did a comparison of their host galaxy colors compared to those BAT AGN not in mergers. A histogram of the merger and non-merger sample is shown in Fig. 9. When separated by color, we find the merging population showing bluer colors and hence increased levels of star formation. This finding is in agreement with Koss et al. (2010) which found a higher rate of specific star formation from the *IRAS* 60 μm fluxes for the merging BAT AGN. We also find that spiral morphologies have bluer average colors than elliptical or intermediate morphologies (Fig. 10).

Since galaxies of different morphologies tend to have
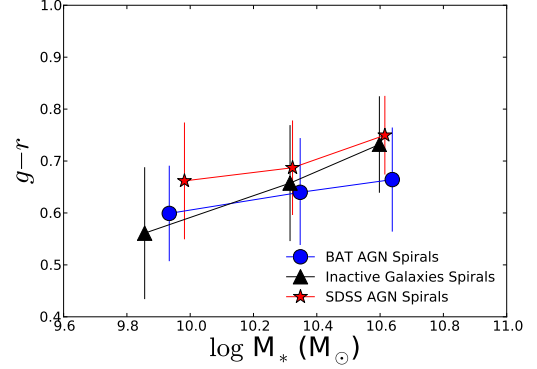
Figure 11. Plot of Petrosian $g-r$ for BAT AGN spirals, inactive galaxy spirals, and SDSS AGN spirals. The error bars indicate standard deviations in each bin. We find a much smaller difference in colors of the three samples when we compare only galaxies with spiral morphologies. We find a similar trend in the $u-r$ colors. This suggests that the higher incidence of spirals in the BAT AGN contributes to the bluer colors found when compared to the SDSS AGN or inactive galaxies.
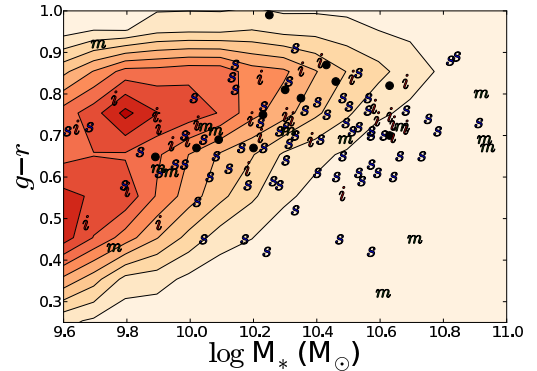
Figure 12. Petrosian $g-r$ of BAT AGN (black dots and letters) and inactive galaxies (contours) plotted as a function of logarithm of the stellar mass (M_*). The contour levels are plotted on a linear scale with each level representing 10% of the data (6875 inactive galaxies). In the BAT AGN sample, m, denotes a galaxy in a merger, s, a spiral morphology, i an intermediate morphology, and black dots denote ellipticals. We find a predominance of BAT AGN in blue, massive spirals and mergers in the regions outside of where most inactive galaxies lie. We find a similar trend in the $u-r$ colors.

different colors, we examined the colors of spirals in the BAT AGN, inactive galaxy, and SDSS AGN samples to look for differences. In Fig. 11, we show a plot of the colors of galaxies classified as spirals in Galaxy Zoo. We find a much smaller difference in colors of the three samples when we compare only galaxies with spiral morphologies. This suggests that the higher incidence of spirals in the BAT AGN sample may largely account for the bluer host galaxy colors when compared to SDSS AGN or inactive galaxies.

A plot showing the color of each BAT AGN and its morphology can be found in Fig. 12. We also show the inactive galaxy colors with contours. We find that the BAT AGN occupy a unique space in color, morphology, and stellar mass by tending to be in massive spirals and mergers that are bluer than massive ellipticals.

In terms of ultra hard X-ray luminosity, we do not find a significant difference between ellipticals, interme-
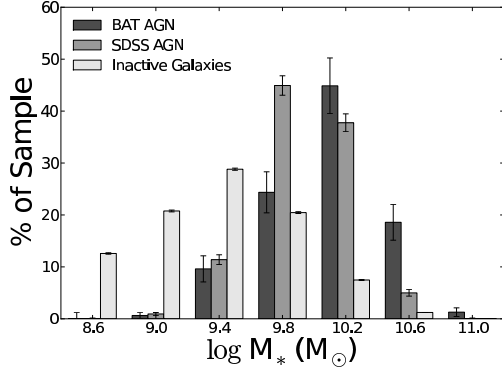
Figure 13. Histogram of stellar masses (M_*) of the BAT AGN sample compared to inactive galaxies and SDSS AGN. The error bars represent 1σ Poisson statistics. The BAT AGN have significantly higher average stellar masses (mean log $M_*=10.27\pm0.4$) than inactive galaxies (9.45 ± 0.58) and slightly higher stellar average stellar masses than SDSS AGN (10.18 ± 0.28).

Figure 14. Plot of average ultra hard X-ray luminosity vs. stellar mass. Error bars represent the standard deviations in each bin. We find greater ultra hard X-ray emission for galaxies with larger stellar mass. A K-S test has $<0.2\%$ probability that the distributions of ultra hard X-ray luminosities are the same for the lowest quartile and highest quartile of stellar mass. In addition, for the average stellar masse, we find a correlation between log $L_{14-195\,keV}$ and log M_* with a slope of 0.62 ± 0.17 and a less than 2% probability that the values are uncorrelated. We have also plotted a line with a linear fit between stellar mass and ultra hard X-ray emission.

diates, or spirals. However, we do find a larger mean ultra hard X-ray emission from BAT AGN in mergers (log $L_{14-195\,keV} =43.64\pm0.48$) when compared to the non-merger sample (log $L_{14-195\,keV} =43.32\pm0.61$. A K-S test indicates a $<5\%$ probability that the ultra hard X-ray emission from AGN in mergers is from the same population as the non-merger sample.

4.4. *Stellar Masses and Ultra Hard X-ray Emission*

We find that the BAT AGN host galaxies are predominantly in the most luminous and massive of galaxies. The mean optical luminosity is higher for BAT AGN (M_r of -21.41±0.82) compared to inactive galaxies (-19.84±1.03), and SDSS AGN (-20.95±0.69)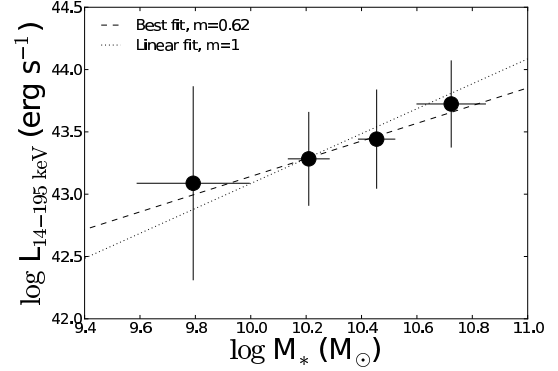. The BAT AGN also have higher mean stellar mass (log $M_*=10.28\pm0.4$) compared to inactive galaxies (9.46 ± 0.58) and SDSS AGN (10.18 ± 0.28). This suggests that the BAT AGN tend to be in more massive galaxies than the SDSS AGN or inactive galaxies. See Fig. 13 for a histogram of the stellar masses of the populations. A K-S test has $<0.01\%$ probability that the BAT AGN stellar masses are from the same population as the inactive galaxies or SDSS AGN. We also confirm that SDSS AGN are in more massive galaxies than inactive galaxies (Kauffmann et al. 2003). We also fit a Schechter function and find that the logarithm of the characteristic stellar mass (M^*) from the best fit is 10.28, 10.02, and 9.89 for the BAT AGN, SDSS AGN, and inactive galaxies in agreement with our findings that BAT AGN are more massive than inactive galaxies or SDSS AGN.

We also find that the average hard X-ray luminosity increases with stellar mass (Fig. 14). The lowest quartile stellar mass has log $L_{14-195\,keV} = 43.07 \pm 0.88$ and the highest quartile stellar mass has log $L_{14-195\,keV} = 43.72\pm 0.36$. In the lowest stellar mass quartile 34% of sources have log $L_{14-195\,keV}$ <43 while in the highest stellar mass quartile none of the sources have log $L_{14-195\,keV}$ <43. A K-S test has $<0.2\%$ probability that the distributions of ultra hard X-ray luminosities are the same for the lowest quartile and highest quartile of stellar mass. In addition, for the average stellar masses, we find a linear correlation between log $L_{14-195\,keV}$ and log M_* with a slope of 0.62 ± 0.14 and a less than 2% probability that

the values are uncorrelated.

4.5. *Tests of Unification Model*

We also tested the Unified Model of Seyferts using the BAT sample. In this model, it is assumed that all AGN are the same types of objects so host galaxy properties such as color, star formation, and morphology should be independent of the Seyfert type or level of obscuration toward the central engine.

We find that the host galaxy colors of narrow and broad-line AGN are the same in agreement with the unification model. Both the $g-r$ and $u-r$ colors of broad-line AGN and NL AGN after GALFIT subtraction for AGN emission are very similar (Fig. 15). For broad-line AGN, the mean $g-r$ is 0.66±0.15 and for NL, the mean $g-r$ is 0.68±0.12 with P(K-S)=43% that the populations are the same. In $u-r$, the color for broad-line AGN is 2.16±0.55 and NL AGN is 2.18±0.61 with P(K-S)=99% that the populations are the same.

An additional test of the Unified Model can be done by checking whether there is any correlation between color and column density in the BAT sample. Column densities were obtained from the literature (Winter et al. 2008, 2009; Bassani et al. 1999; Noguchi et al. 2010) and the Tartarus database. We see no correlation between column density and host galaxy color (Fig. 16). Since host galaxy color measures the relative amount of star formation, this suggest that there is no relation between X-ray column density (N_H) and star formation.

We also investigated whether the NL and broad-line AGN have different rates of star formation in the far-IR. We define a proxy for specific star formation rate as the logarithm of the ratio of 90 μm emission from *AKARI* to stellar mass. The mean value for this parameter for the narrow-line AGN is 33.6±0.4 erg s$^{-1}M_\odot^{-1}$ and for broad-line AGN is 33.4±0.4 erg s$^{-1}M_\odot^{-1}$. A K-S test indicates a 35% probability that the rates of specific star formation for the narrow and broad-line AGN are the same in agreement with the Unified Model of AGN.

In addition, we compared the morphologies of broad
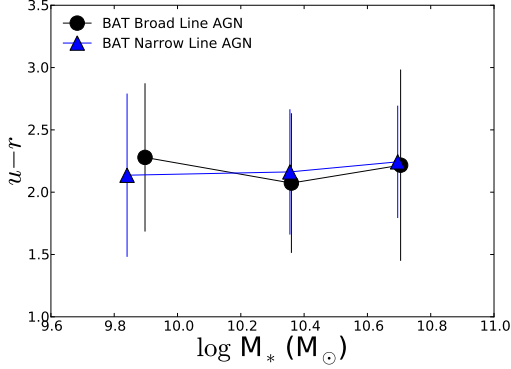
Figure 15. Comparison of average BAT AGN host galaxy colors separated by broad-line and narrow-line. The error bars indicate standard deviations in each bin. Petrosian $u - r$ by stellar mass (M_*) for broad-line and narrow-line AGN in the BAT sample. Both narrow-line and broad-line AGN show similar host galaxy colors in agreement with AGN unification with P(K-S)= 99% and 36% for $u - r$ and $g - r$ respectively.
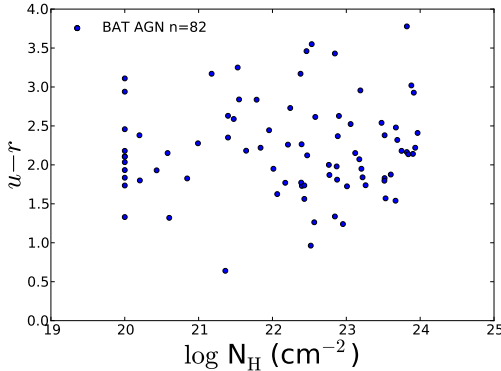
Figure 16. Scatter plot of X-ray column density vs. host galaxy $u - r$. We see no correlation of X-ray column density with host galaxy color in agreement with AGN unification. We also find no correlation in $g - r$.

and narrow-line AGN. Because of the difficulty of determining morphology class for galaxies with very bright AGN, we limited our sample to galaxies with %PS_r < 35. A plot of the percentage in each sample of different types of morphology can be found in Fig. 17. We see no difference in the morphologies of broad and narrow-line AGN.

Finally, we compared the axis ratios of BAT AGN with different optical classifications and obscuring column densities. In the unified model of Seyferts, the observed X-ray spectra of Seyfert 2s are expected to have higher absorbing column density than Seyfert 1s due to an edge-on view of the obscuring torus. However, edge-on spirals have been shown to have a geometrically thick layer of obscuring material in the host-galaxy planes that can also increase the absorbing column density (Simcoe et al. 1997). We confirm this by finding more NL AGN in highly inclined systems with smaller axis ratios (b/a<0.4; Fig. 18, left). We also compared X-ray column density vs. host galaxy inclination and found more inclined systems tend to have higher average X-ray column densities (Fig. 18, right). This finding confirms an earlier result from the smaller 9-month sample of BAT
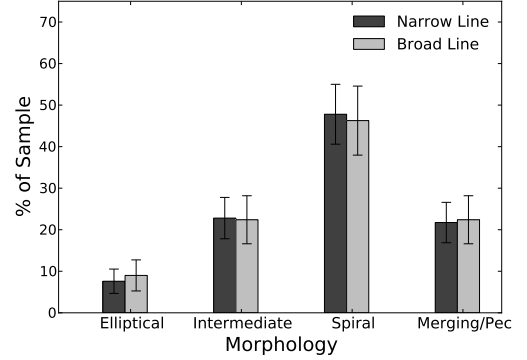
Figure 17. Comparison of BAT AGN host galaxy morphologies separated by broad and narrow-line AGN. The error bars represent 1σ Poisson statistics. We see no difference in the morphologies of the two samples in agreement with AGN unification.
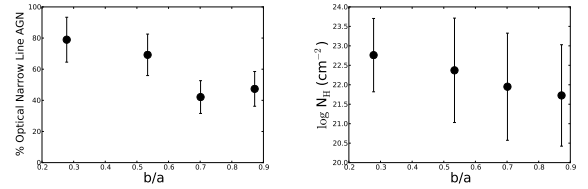
Figure 18. *Left*: Percent of narrow-line AGN vs. host galaxy inclination as measured by the axis ratio (b/a). The error bars indicate standard deviations in each bin. Galaxies with lower axis ratios tend to be more edge on. We find more NL AGN in highly inclined systems with smaller axis ratios. *Right*: X-ray column density vs. host galaxy inclination as measured by the axis ratio (b/a). The error bars indicate standard deviations in each bin. Galaxies with higher inclinations have a higher mean X-ray column density. A K-S test indicates a <5% probability that the X-ray column densities from the lowest and highest distributions of axis ratios are from the same parent population.

AGN (Winter et al. 2009).

5. SUMMARY AND DISCUSSION

We have assembled the largest sample of ultra hard X-ray selected AGN with host galaxy optical data to date, with 185 AGN in total. We have performed extensive modeling with GALFIT to effectively remove the AGN light from the optical images. Using optical photometry, morphology, and spectroscopy, along with FIR emission we found:

(i) The BAT AGN galaxies are bluer in optical color than inactive galaxies or SDSS Seyferts of the same stellar mass.

(ii) We find a much higher incidence of spiral morphologies in BAT AGN compared to SDSS AGN or inactive galaxies. Amongst massive galaxies (log $M_* > 10.5$), the BAT AGN show a preference for spiral morphologies that is 5 to 10 times higher than SDSS AGN or inactive galaxies. We also find that the bluer colors of BAT AGN can be accounted for by a higher fraction of mergers and spirals.

(iii) The BAT AGN have greatly enhanced 90 μm emission compared to inactive galaxies or SDSS Seyferts matched in redshift and stellar mass.

(iv) The BAT NL AGN have similar intrinsic [O III] $\lambda5007$ luminosities as NL SDSS Seyferts of the same redshift range.

(v) The BAT AGN are found in the most massive host galaxies with high concentration indexes indicative of large bulge-to-disk ratios and large supermassive black holes.

(vi) We also find that the average ultra hard X-ray luminosity increases with stellar mass and that BAT AGN in mergers have greater ultra hard X-ray emission than those in other morphological types. This suggests a link between supermassive black hole growth and the mass of the host galaxy.

(vii) In agreement with the Unified Model of AGN, we find the host galaxy colors and morphology are independent of X-ray column density and optical Seyfert classification.

These results indicate that host galaxy morphology is related to the activation and fueling of local AGN. Ultra hard X-ray selected AGN are particularly associated with massive spiral galaxies and galaxy mergers. These types of objects are generally associated with bluer colors, compared to the red massive early-type galaxies at similar stellar masses. These observational results provide some evidence for an association between AGN activity and galaxy mergers (e.g., di Matteo et al. 2005), and also provide examples of AGN activity driven by the stochastic accretion of cold gas that should be more prominent among late-type systems (Hopkins & Hernquist 2006).

Recent simulations have also suggested a transition between the fueling mechanisms of AGN with nonmerger events predominantly powering lower luminosity AGN and merger-induced fueling dominant in more luminous quasars (Hopkins & Hernquist 2009). We may be seeing evidence of this transition in our sample of BAT AGN that is powered both through merger events and less powerful nonmergers such as accretion of cold gas in late type systems. In support of this, we find that BAT AGN in mergers have a greater ultra hard X-ray emission than those in other morphological types. However, only a very small fraction (5/185) of BAT AGN in this sample are above the minimum bolometric luminosity associated with quasars ($L_{bol} > 10^{45}$ erg s^{-1}). These results suggest that the process of merging may be important for powering more moderate luminosity AGN as well (see also Koss et al. 2010).

In interpreting the results of an X-ray flux limited survey, it is useful to remember that the observed flux is a product of the black hole mass and accretion rate. On average, more massive galaxies will tend to have higher mass black holes that will produce a larger average X-ray flux than smaller galaxies with on average smaller black holes. However, among massive galaxies, elliptical morphologies are much more common than spirals, yet we find the most luminous hard X-ray AGN almost exclusively in spiral morphologies. This suggests that spiral morphologies must have higher accretion rates than elliptical morphologies. This finding is in agreement with recent theoretical predictions that suggest that only spirals typically have enough gas to trigger higher levels of radiatively efficient accretion in a geometrically thin disk

(Fanidakis et al. 2011). In order to understand this further, we are in the process of accurately measuring black hole masses to study the accretion rates for this sample.

Previous optical surveys have found that AGN tend to be in massive galaxies (Kauffmann et al. 2003), occur along the red sequence (Westoby et al. 2007), and tend to have similar numbers of galaxy mergers as inactive galaxies (Li et al. 2006). However, in an ultra hard X-ray survey of AGN, we find that AGN host galaxies are bluer than inactive galaxies with higher numbers of massive spirals and galaxy mergers. We do not find observational evidence that the AGN suppresses star formation.

It is surprising that the optical morphologies and colors of ultra hard X-ray selected AGN are so different than emission line selected Type 2 Seyferts given their similar bolometric luminosity as measured in [O III]. However, these results are consistent with recent Spitzer surveys that have found that the AGN detection rate in late-type galaxies and mergers is much larger than what optical spectroscopic observations suggest (Satyapal et al. 2008; Goulding & Alexander 2009; Veilleux et al. 2009b). Finally, studies of X-ray selected AGN at higher redshifts, have also found a significant population of AGN classified as star forming using emission line diagnostics (Yan et al. 2011, accepted).

In the BAT AGN sample, there are several results that suggest optical emission line classification may be biased against late-type galaxies and mergers. In this study, we found that the axis ratios of BAT AGN are in general more inclined and have greater levels of internal extinction than comparable SDSS AGN. This extinction could obscure or dilute the narrow-line region and cause AGN galaxies to be misclassified as star forming regions. This finding is also in agreement with a previous analysis of BAT AGN that found optical emission line diagnostics preferentially misclassify merging AGN because of optical extinction and dilution by star formation (Koss et al. 2010).

Another possibility is that the BAT AGN may be much more intrinsically luminous than their [O III] emission suggests. Since the majority of BAT AGN either have broad lines or are NL AGN that are correctly classified as Seyferts, yet are found to have much greater hard X-ray luminosities, this must be an important factor. In support of this, two studies of BAT AGN have found a very weak correlation between the [O III] and hard X-ray luminosity and that BAT AGN have additional reddening of the narrow line region not accounted for in optical studies (Winter et al. 2010; Meléndez et al. 2008). This is also supported by the much greater number of narrow-line SDSS Seyferts compared to hard X-ray selected AGN. In the SDSS survey area, there are 24 optical emission line selected narrow-line Seyferts detected for each hard X-ray AGN at the same redshift. Some of these undetected sources may be heavily absorbed Compton-Thick AGN missed in the hard X-rays, but even the highest estimates expect only $\approx 50\%$ of local narrow-line AGN are Compton Thick (Risaliti et al. 1999). If the BAT AGN are intrinsically more luminous than emission line selected AGN, this may explain their higher rates of mergers and enhanced FIR emission. We are currently in the process of assembling a larger survey of optical spectra of BAT AGN to better understand optical and X-ray measures of intrinsic luminosity.

6. ACKNOWLEDGEMENTS

REFERENCES

Ajello, M., et al. 2008, ApJ, 673, 96
Bassani, L., Dadina, M., Maiolino, R., Salvati, M., Risaliti, G., della Ceca, R., Matt, G., & Zamorani, G. 1999, ApJSS, 121, 473
Bernardi, M., et al. 2003, AJ, 125, 1849
Bertin, E., & Arnouts, S. 1996, A&AS, 117, 393
Blanton, M. R., et al. 2001, AJ, 121, 2358
Blanton, M. R., & Roweis, S. 2007, AJ, 133, 734
Bruzual, G., & Charlot, S. 2003, MNRAS, 344, 1000
Calzetti, D., Armus, L., Bohlin, R., Kinney, A., Koornneef, J., & Storchi-Bergmann, T. 2000, ApJ, 533, 682
Cardelli, J. A., Clayton, G. C., & Mathis, J. S. 1989, ApJ, 345, 245
Chabrier, G. 2003, PASJ, 115, 763
Dekel, A., et al. 2009, Nature, 457, 451
di Matteo, T., Springel, V., & Hernquist, L. 2005, Nature, 433, 604
Fanidakis, N., Baugh, C. M., Benson, A. J., Bower, R. G., Cole, S., Done, C., & Frenk, C. S. 2011, MNRAS, 410, 53
Gavazzi, G., Franzetti, P., Scodeggio, M., Boselli, A., & Pierini, D. 2000, A&A, 361, 863
Goulding, A. D., & Alexander, D. M. 2009, MNRAS, 398, 1165
Haubler, B., Barden, M., & McIntosh, D. H. 2008, AIPC, 1082, 137
Heckman, T. M. 1980, A&A, 87, 152
Hickox, R. C., et al. 2009, eprint arXiv, 0901, 4121
Ho, L. C., Filippenko, A. V., Sargent, W. L. W., & Peng, C. Y. 1997, ApJS, 112, 391
Hopkins, P. F., & Hernquist, L. 2006, ApJSS, 166, 1
—. 2009, ApJ, 694, 599
Kauffmann, G., et al. 2003, MNRAS, 346, 1055
Kewley, L. J., Groves, B., Kauffmann, G., & Heckman, T. 2006, MNRAS, 372, 961

Kewley, L. J., Heisler, C. A., Dopita, M. A., & Lumsden, S. 2001, ApJSS, 132, 37
Kim, M., Ho, L. C., Peng, C. Y., Barth, A. J., Im, M., Martini, P., & Nelson, C. H. 2008, ApJ, 687, 767
Kirhakos, S. D., & Steiner, J. E. 1990, AJ, 99, 1435
Koss, M., et al. 2011, ApJL, 735, L42
Koss, M., Mushotzky, R., Veilleux, S., & Winter, L. 2010, ApJL, 716, L125
Kriek, M., van Dokkum, P. G., Labbé, I., Franx, M., Illingworth, G. D., Marchesini, D., & Quadri, R. F. 2009, ApJ, 700, 221
Levine, A. M., et al. 1984, ApJSS, 54, 581
Li, C., Kauffmann, G., Wang, L., White, S. D. M., Heckman, T. M., & Jing, Y. P. 2006, MNRAS, 373, 457
Lintott, C. J., et al. 2008, MNRAS, 389, 1179
Lupton, R., Blanton, M. R., Fekete, G., Hogg, D. W., O'Mullane, W., Szalay, A., & Wherry, N. 2004, PASJ, 116, 133
Magorrian, J., et al. 1998, AJ, 115, 2285
Malizia, A., Stephen, J. B., Bassani, L., Bird, A. J., Panessa, F., & Ubertini, P. 2009, MNRAS, 399, 944
Maller, A. H., Berlind, A. A., Blanton, M. R., & Hogg, D. W. 2009, ApJ, 691, 394
Masters, K. L., et al. 2010, MNRAS, 404, 792
Meléndez, M., et al. 2008, ApJ, 682, 94
Mink, D. J. 1996, Astronomical Data Analysis Software and Systems V, 101, 96
Mulchaey, J. S., & Regan, M. W. 1997, ApJL, 482, L135
Mullaney, J. R., Alexander, D. M., Goulding, A. D., & Hickox, R. C. 2011, MNRAS, 414, 1082
Mushotzky, R. 2004, Supermassive Black Holes in the Distant Universe. Edited by Amy J. Barger, 308, 53
Netzer, H., et al. 2007, ApJ, 666, 806
Noguchi, K., Terashima, Y., Ishino, Y., Hashimoto, Y., Koss, M., Ueda, Y., & Awaki, H. 2010, ApJ, 711, 144
Patton, D. R., & Atfield, J. E. 2008, ApJ, 685, 235
Peng, C. Y., Ho, L. C., Impey, C. D., & Rix, H.-W. 2002, AJ, 124, 266
Pierce, C. M., et al. 2010, MNRAS, 405, 718
Richards, G. T., et al. 2006, ApJSS, 166, 470
Risaliti, G., Maiolino, R., & Salvati, M. 1999, ApJ, 522, 157
Satyapal, S., Vega, D., Dudik, R. P., Abel, N. P., & Heckman, T. 2008, ApJ, 677, 926
Schawinski, K., et al. 2010, ApJ, 711, 284
Schawinski, K., Virani, S., Simmons, B., Urry, C. M., Treister, E., Kaviraj, S., & Kushkuley, B. 2009, ApJL, 692, L19
Schlegel, D. J., Finkbeiner, D. P., & Davis, M. 1998, ApJ, 500, 525
Silverman, J. D., et al. 2008, ApJ, 675, 1025
Simcoe, R., McLeod, K. K., Schachter, J., & Elvis, M. 1997, ApJ, 489, 615
Simmons, B., & Urry, C. 2008, ApJ, 683, 644
Smith, J. A., et al. 2002, AJ, 123, 2121
Stern, D., et al. 2005, ApJ, 631, 163
Tueller, J., et al. 2010, ApJS, 186, 378
Tueller, J., Mushotzky, R. F., Barthelmy, S., Cannizzo, J. K., Gehrels, N., Markwardt, C. B., Skinner, G. K., & Winter, L. M. 2008, ApJ, 681, 113
Vasudevan, R. V., Mushotzky, R. F., Winter, L. M., & Fabian, A. C. 2009, MNRAS, 399, 1553
Veilleux, S., et al. 2006, ApJ, 643, 707
—. 2009a, ApJ, 701, 587
—. 2009b, ApJS, 182, 628
Weedman, D. W. 1977, ARA&A, 15, 69
Westoby, P. B., Mundell, C. G., & Baldry, I. K. 2007, MNRAS, 382, 1541
Winter, L., Mushotzky, R., Tueller, J., & Markwardt, C. 2008, ApJ, 674, 686
Winter, L. M., Lewis, K. T., Koss, M., Veilleux, S., Keeney, B., & Mushotzky, R. F. 2010, ApJ, 710, 503
Winter, L. M., Mushotzky, R. F., Reynolds, C. S., & Tueller, J. 2009, ApJ, 690, 1322

APPENDIX

AGN SUBTRACTION AND GALFIT ANALYSIS

The AGN color is bluer than the host galaxy, so it is important to accurately subtract the AGN light before doing photometry of the host galaxy. Two-dimensional surface brightness fitting was done using GALFIT (Peng et al. 2002) in the $ugriz$ band to measure and subtract the AGN light. The program can simultaneously fit an arbitrary number of components using χ^2 minimization to determine the best-fit parameters. Our choice of GALFIT is based on the recent comparison of GIM2D vs. GALFIT which showed better fitting results and stability in finding solutions (Haubler et al. 2008). While the median atmospheric seeing of our sample was only $\approx 1.5''$, since the sample is at a very low redshift, this ground-based optical imaging is comparable or even superior to the best Hubble Space Telescope (HST) images at high-redshift (z>0.5).

Initial estimates of galaxy magnitude, position, position angle, axis ratio, and half-light radius were provided using SExtractor following the GALAPOGOS routine (Haubler et al. 2008). A point source (PS) was used to fit the AGN light. The Point Source Function (PSF) was modeled using five coadded bright stars in the same image field as the galaxy. An initial run of GALFIT was done using only a PS component to replace the SExtractor inputs for central position and PS magnitudes. Sky background estimates were made using SDSS sky values or from SExtractor.

To model the galaxy light we used the Sérsic profile, which is an exponential function with a variable half-light radius and an exponential parameter, n, called the Sérsic index (Sérsic 1968). For n=1, the Sérsic profile is the same as an exponential disk model. When n=4, the Sérsic profile is the same as a de Vaucouleurs bulge. Other authors have used different fixed and floating Sérsic index models including a fixed bulge (n=4), a fixed disk and bulge (n=1 and n=4), and a floating Sérsic index (Veilleux et al. 2006, 2009a; Schawinski et al. 2009). While a detailed study of the most effective way to measure the AGN and galaxy light has been done for simulated HST images (Simmons & Urry 2008; Kim et al. 2008; Pierce et al. 2010), little has been done for ground-based images similar to the current study. Therefore, to determine the best modeling approach with GALFIT and the associated error, we simulated AGN galaxies for both our Kitt Peak and SDSS images.

To determine the best model to measure the AGN and galaxy light, we simulated broad-line AGN galaxies by adding bright stars to the centers of images of inactive galaxies and NL AGN. We randomly selected one star from our images to use as the simulated AGN PS and placed it in the center of the galaxy. Since the SDSS and Kitt Peak data had different PSFs and exposure times, we tested them separately. To test the SDSS data, we selected 15 inactive galaxies from the SDSS catalog which matched in redshift, color, and apparent magnitude to our Seyfert 2 galaxies with $0.025 < z < 0.05$. These galaxies are the most distant in our sample and have the poorest resolution, so PS subtraction leads to large errors; they therefore serve as a worst case scenario for our sample. For the Kitt Peak images we chose a sample of 10 of the BAT Seyfert 2 galaxies with the same redshift range. For each of the simulated AGN galaxies we added the star at incremental percentage ($\%PS_r$) values of total (AGN and galaxy) light in the r band. In total, to test them in each filter, we created 300 simulated AGN galaxies and ran GALFIT 3500 times. We then used these simulated AGN galaxies to test the effectiveness of GALFIT with different models.

Fig. 19 shows the simulation results for the different Sérsic models for increasing $\%PS_r$ light in the r band. We did not find a significant difference in GALFIT modeling using the Kitt Peak or SDSS samples, so these results include both samples. We found an inaccurately modeled PSF will force GALFIT to converge to artificially high Sérsic indexes for the galaxy model. This has also been found in simulated HST images (Simmons & Urry 2008; Kim et al. 2008). The PSF mismatch causes light from the host galaxy component to be artificially increased by effectively taking light from the AGN component. This happens by inflating the galaxy Sérsic index. This effect increases as the $\%PS_r$ increases. In addition, as we move towards larger $\%PS_r$, the associated standard deviation of error of the modeled galaxy light increases.

To accurately remove the AGN light, it is important to choose the best model. We did this by finding the difference between the modeled galaxy light and the actual galaxy light. When no PS component is used in the models, GALFIT still finds a faint AGN, so after subtraction, the modeled galaxy light component is fainter than the actual one. When the host galaxy is brighter than the AGN in the r band ($\%PS_r<50$), the worst model is to simply subtract a PS component to estimate the galaxy light because this overestimates the AGN light. For the Sérsic and PS fitting models, the best model is to use an n=4 fixed bulge component and PS or n<4 variable Sérsic Index and PS since these models have the smallest average error and standard deviation of error. The worst model is fitting with a disk(n=1) and bulge(n=4) or fitting with a variable Sérsic Index since these models have the largest average overestimation of galaxy light and have the largest standard deviation of error. Simmons & Urry (2008) also found this result using simulated HST images. To avoid any systematic biases against disk-like systems we used the n<4 variable Sérsic Index although the fixed bulge (n=4) Sérsic model performed similarly. An initial guess of 2.5 was used for the Sérsic Index. The index was allowed to float in the model along with all other values other than the sky background.

The next step was to broaden the examination of GALFIT's performance from one filter to the entire $ugriz$ filter set. In Fig. 20 (left), we show the performance in each of the filters. They are similar to each other, but the blue bands have higher uncertainties because of poorer resolution.

When testing the performance across filters it is important to consider that the AGN spectral energy distribution (SED) emits more energy at bluer wavelengths than the host galaxy; otherwise we may underestimate the contamination in the bluer bands. To examine this, we assumed a AGN SED power law of $f_\nu^{-0.5}$ as has been found for the optical spectrum of quasars (Richards et al. 2006). We then normalized to the total light in each filter band based off of the $\%PS_r$.
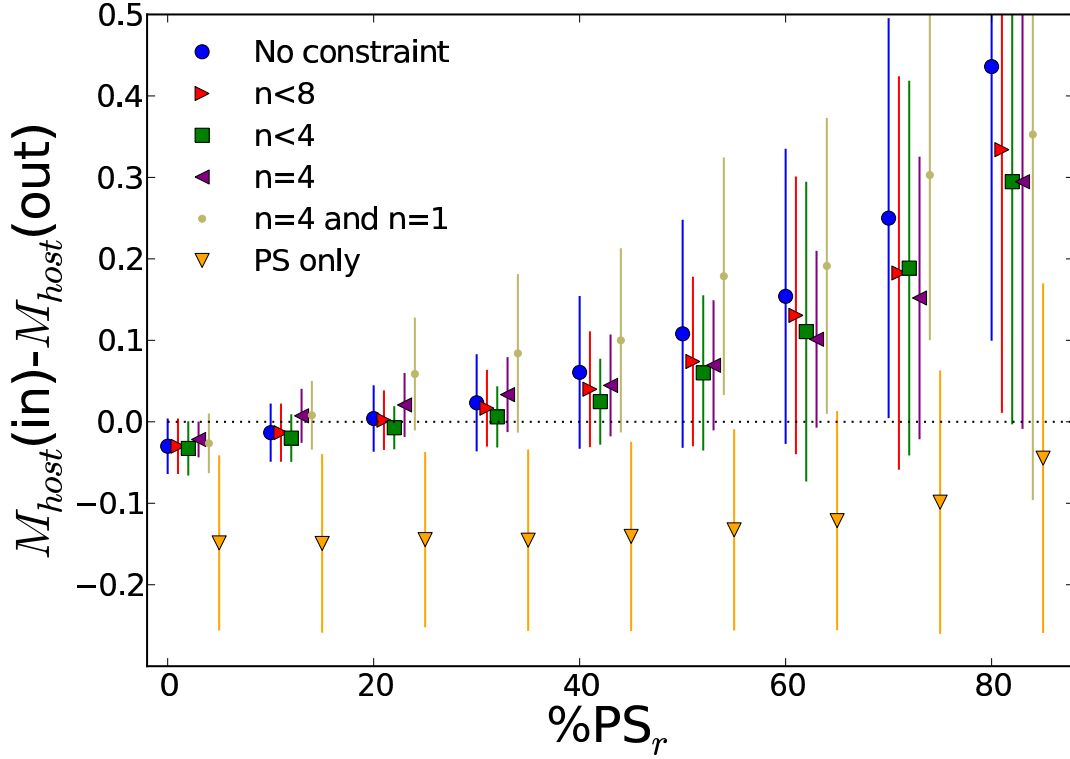
Figure 19. To determine the best models to use for subtraction of the AGN light, we tested simulated AGN galaxies using different Sérsic models with a point source (PS) to fit the AGN light. We varied the AGN to total light (%PS$_r$) in the r band to test how the models performed at increasing levels of AGN light. A positive value indicates that the mean host galaxy light is overestimated. The error bars indicate standard deviations in each bin. As the (%PS$_r$) increases the host galaxy light is overestimated by all of the Sérsic and PS models and the standard deviation increases. We find that the model with a PS and floating Sérsic Index with n<4 or n= 4 is most effective at measuring the AGN light based on a lower measured AGN contamination and smaller standard deviation.

These final modeling results suggest important constraints where GALFIT is effective in removing the AGN light (Fig. 20, right). Based on these results, we restrict our u band photometry to galaxies with AGN brightnesses of %PS$_r$<20 where the contamination is 0.05±0.15 mag. For photometry in the other $griz$ filters, a less stringent restriction of %PS$_r$<40 is sufficient to keep our errors within $\sigma = 0.05\pm0.04$ mag.

In addition to our simulations, we also tested the real BAT AGN galaxies for AGN contamination after removing the AGN light measured by GALFIT. The effects of subtracting the AGN contribution with GALFIT are shown for the $u-r$ and $g-r$ for the broad-line AGN in Fig. 21. The galaxy colors stay flat with increasing % of AGN light up to ≈20% for the u band and ≈35% for the $griz$ band. This agrees with the results of our modeling of AGN contamination at 20% for the u band and 40% for the $griz$. Based on these results, we have imposed a tighter restriction of 35% AGN light on the $griz$ band photometry to ensure there is no AGN contamination.

We have restricted our color analysis of host galaxies because of our inability to remove the AGN light with GALFIT for the brightest AGN. After fitting with GALFIT, 17 or 10% of galaxies had bright broad-line AGN, where %PS$_r$>35, and these galaxies were not included in the $griz$ analysis because of uncertainty of the host galaxy photometry (Fig. 22). When we include both the galaxies that were not included because of pixel saturation and those with with %PS$_r$>35, the completeness is 71% for the highest quartile of BAT luminosity and >95% for the other 3 quartiles. In the u band, 41 galaxies or 23% were excluded because the luminosity of the AGN exceeded 20%. The completeness is 71% for the highest quartile of BAT luminosity and >95% for the other 3 quartiles. This may introduce a small bias against QSO-like systems. However, in the regions where GALFIT is accurate in the removal of the AGN, we do not see any strong trends towards bluer colors in higher luminosity AGN.

Our photometry will be used to provide colors and stellar masses of the host galaxy. Contamination from the AGN will be reduced in relative color measurements, since the photometry from all filters includes light from the AGN and will to some extent be subtracted off in color measurements. Finally, when using photometry to determine stellar masses, the redder bands are weighted more heavily, as they tend to be less contaminated by the AGN component than the bluer bands.
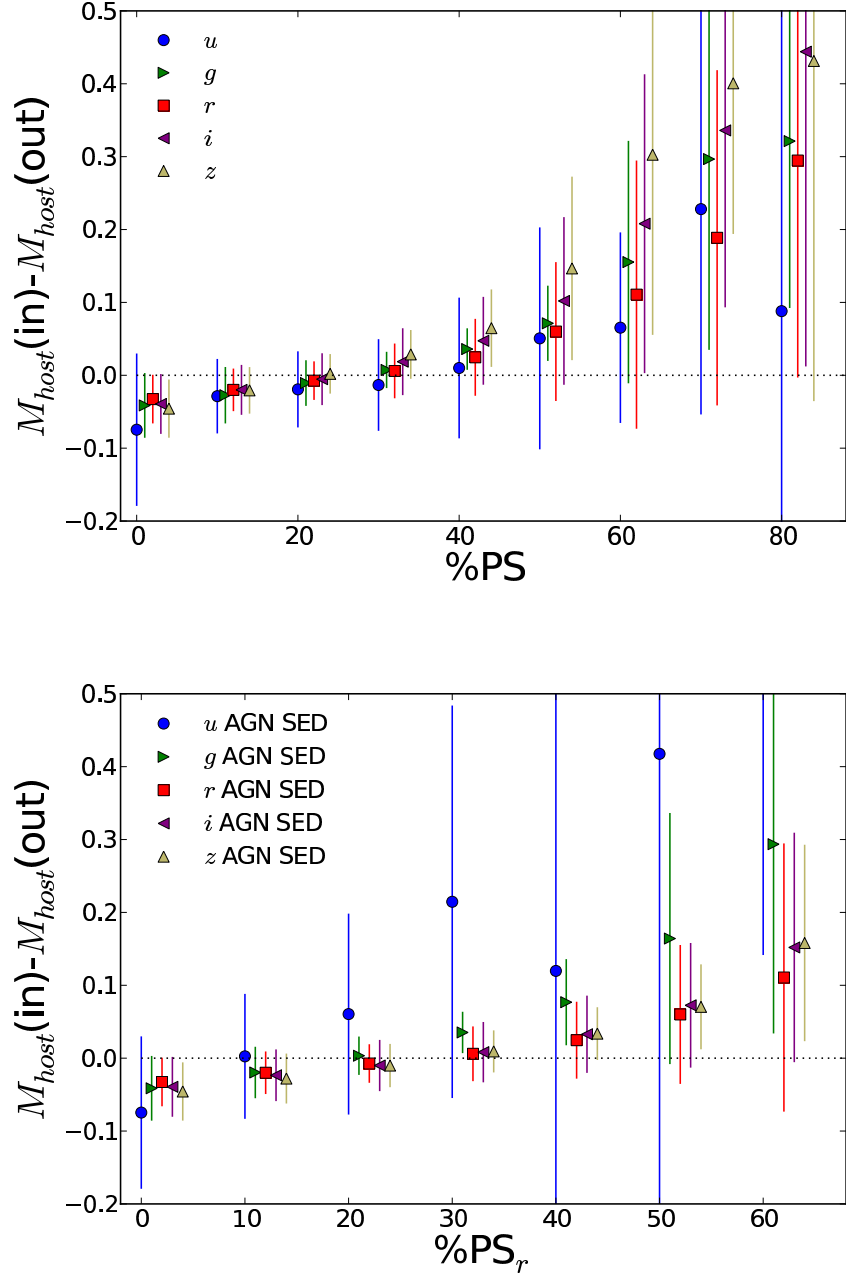
Figure 20. *Top*: Effectiveness of GALFIT in removing the AGN light by filter for modeled AGN galaxies. We have used a PS and floating Sérsic Index with n<4 to measure the AGN light. Increasing levels of %PS are shown. As the simulated AGN light increases, the galaxy light is overestimated for all filters. The error bars indicate standard deviations in each bin. The errors are higher for the u and z where the resolution is poorer. *Bottom*: We also included the effect of the bluer quasar SED using the colors of AGN (Richards et al. 2006) and the colors of our average Seyfert 2 host galaxy. The error bars indicate standard deviations in each bin. The bluer filter performance is worse because of the higher ratio of AGN to galaxy light.

COMPARISON SAMPLE

In this section, we discuss considerations in our choice of the comparison sample from the SDSS, the use of catalog photometry, and importance of comparing galaxies with similar brightnesses or stellar masses. We have used galaxies with both photometry and spectroscopy from the SDSS as a comparison sample. Since 50% (93/185) of BAT AGN galaxies are in the SDSS spectroscopic coverage area, we can examine these galaxies to determine the completeness of the SDSS catalog sample. In Fig. 23, the SDSS spectroscopic coverage of BAT AGN by redshift bin is shown. While 70% of the BAT sample in the SDSS has spectroscopic coverage, the brightest galaxies in each redshift bin are missed for z<0.03. Above this redshift a few broad-line AGN with bright nuclei are misclassified as stars. Due to the selection effect against the brightest galaxies, in this study we have chosen a SDSS control sample of galaxies with 0.01<z<0.07.
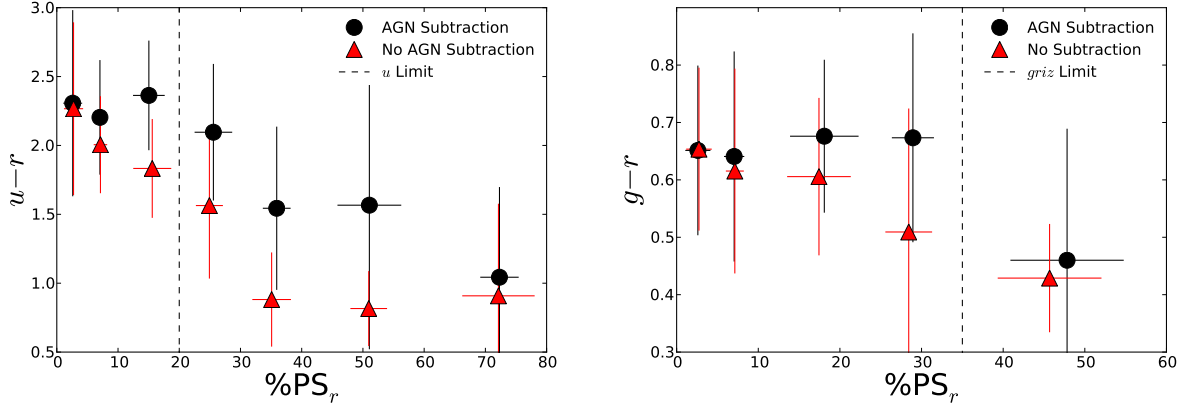
Figure 21. *Left*: Average colors in $u-r$ for BAT AGN before and after AGN subtraction with GALFIT. The error bars indicate standard deviations in each bin. Using GALFIT for AGN subtraction, the colors are almost constant for %PS$_r$ <20. Based on our modeling we believe the strong blueward shift above 20% is due to AGN contamination not accounted for from GALFIT. *Right*: Average colors in $g-r$ for BAT AGN before and after AGN subtraction with GALFIT. The error bars indicate standard deviations in each bin. The ratio of AGN to galaxy light is smaller in g than u and we see a constant color to %PS$_r$ <35.
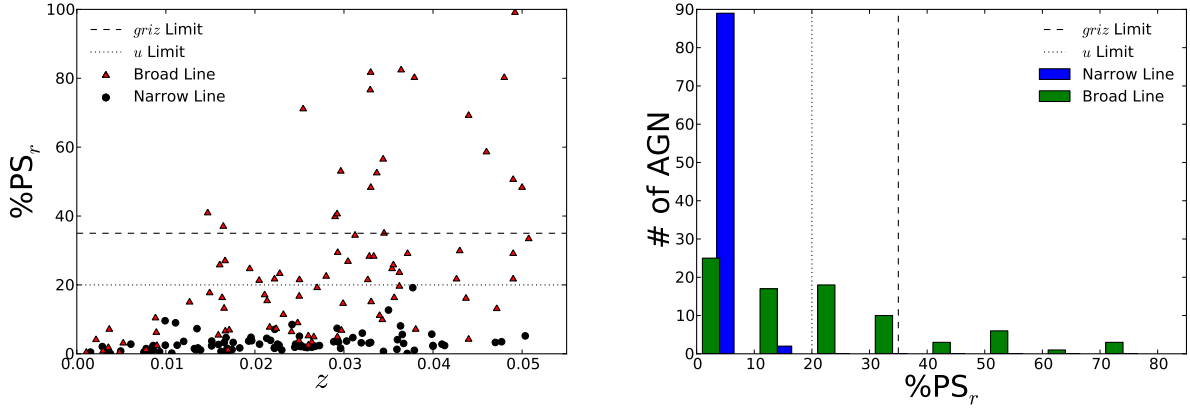
Figure 22. *Left*: Plot of %PS$_r$ for BAT AGN galaxies by redshift. Narrow-line AGN are represented as dots and broad-line AGN are indicated by triangles. Dashed lines indicate the limits above which GALFIT was unable to effectively remove the AGN light. These galaxies were not included in the analysis of colors because of AGN contamination. At higher redshifts we find more BAT AGN with higher ratios of AGN to galaxy light. *Right*: Plot of number of AGN in bins of %PS$_r$. We find that GALFIT finds %PS$_r$ <5 for most BAT narrow-line BAT AGN.
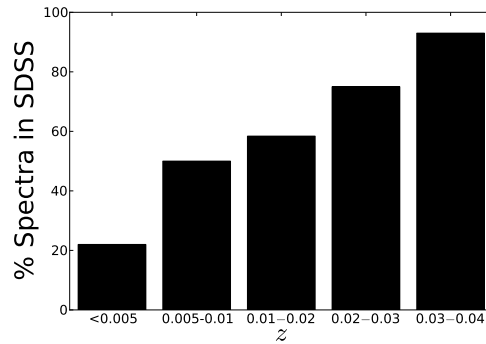
Figure 23. Percent coverage of BAT AGN in the SDSS spectroscopic footprint with spectroscopy. Due to the brightness limits (m$_r$ < 15) in the spectroscopic sample, 30% of the BAT AGN galaxies are missed by the SDSS spectroscopic sample. In addition, some broad-line AGN with bright nuclei are misclassified as stars and not included in the SDSS spectroscopy. Finally, some merging BAT AGN galaxies are not covered because of fiber collision limits in the SDSS. Due to this effect, we have used SDSS galaxies in the redshift range of 0.01<z<0.07 to compare to BAT AGN.
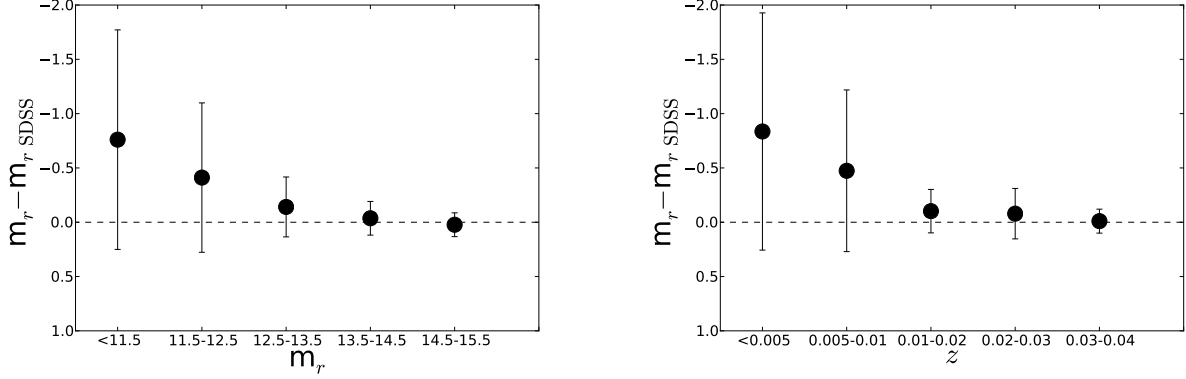
Figure 24. Comparison of our measured Petrosian magnitudes to the SDSS catalog values for a range of magnitudes (m_r) (*left*) and redshifts (*right*). Negative values indicate we find a brighter magnitude than the SDSS catalog. Since the automated routine in the SDSS has a tendency to shred galaxies into multiple component galaxies, the magnitudes are reduced. This shredding effect is much stronger for the brightest galaxies. However, for $m_r > 13.5$ or $z > 0.01$ the magnitudes are in good agreement. Given these results, we have restricted our SDSS catalog comparison to this range.
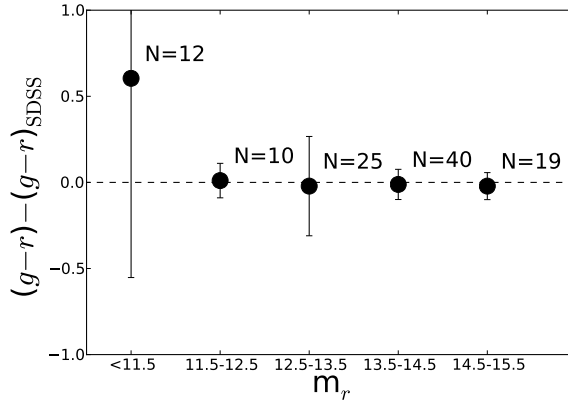
Figure 25. Comparison of the average difference in $g - r$ color between our measurements and the SDSS catalog. The error bars indicate standard deviations in each bin. The SDSS catalog colors show better agreement than apparent magnitudes since the effects of shredding tend to cancel each other out in the reduced brightness of both filters.

We also ensured that our own photometry of BAT AGN agreed with the SDSS catalog measurements. We can measure the differences between our photometry and those in the SDSS catalog since 62% (116/185) of BAT AGN are in the SDSS photometric catalog (Fig. 24). The SDSS photometric catalog incorrectly shreds features of bright, nearby galaxies, such as spiral arms, rings, and dust lanes into different components. This causes a systematic underestimation of the brightness of galaxies and variations in their measured color. Because of this shredding effect, we have restricted our SDSS catalog comparison to galaxies with $m_r > 13.5$ and $z > 0.01$, where we find good agreement in photometry. In Fig. 25, we show a comparison between the $g - r$ of BAT AGN measured in the SDSS catalog and measured using our own photometry. The SDSS catalog colors show better agreement than the photometry since the effects of shredding tend to cancel each other out in relative color measurements.

When comparing host galaxy properties, it is important to consider the flux limited nature of both the SDSS and BAT surveys. In Fig. 26, a plot of average M_r by redshift for the BAT AGN, SDSS AGN, and inactive SDSS galaxies is shown. At higher redshifts the SDSS detects AGN and galaxies that are more luminous and have a higher stellar mass because of a selection effect against optically faint galaxies. On the other hand, the BAT AGN survey detects AGN galaxies of a constant optical brightness across a range of redshifts. Due to these selection effects, it is important to compare host galaxy colors between the BAT survey and SDSS survey only at similar brightnesses or stellar masses.

SELECTION EFFECTS IN THE BAT SURVEY

In the ultra hard X-rays, the BAT survey is also flux limited. Assuming the ultra hard X-ray AGN are distributed randomly following the distribution of luminosities at lower redshifts, and using the limiting sky sensitivity, we can make a further estimate of completeness (Fig. 27). We find that the BAT sources are complete for $z < 0.05$ in this survey for $\log L_{14-195\,\mathrm{keV}} > 43.7$ or $\approx \log L_{2-10\,\mathrm{keV}} > 43.2$ assuming no intrinsic absorption. In addition, we limited our analysis of morphologies to NL BAT AGN. The completeness fractions are shown in Fig. 28 as a function of ultra hard
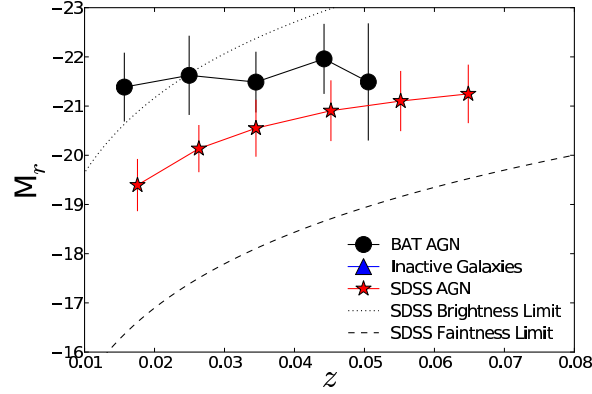
Figure 26. Plot of average absolute mag in r for the BAT AGN, SDSS AGN, and inactive galaxies. The error bars indicate standard deviations in each bin. The dashed lines indicate the approximate brightness and faintness limits from the SDSS spectroscopic survey. At higher redshifts, the SDSS detects galaxies that are more luminous and have a higher stellar mass because of the selection effect against faint galaxies. On the other hand, the BAT AGN survey detects AGN galaxies of a constant optical brightness across a range of redshifts. Due to the selection effects it is important to compare host galaxy colors between the BAT survey and SDSS survey only at similar brightnesses or stellar masses. For comparison, in the redshift range between 0.03 to 0.05 and the survey coverage area of the SDSS, the BAT survey has 28 broad-line and 17 NL AGN. In this same range, the SDSS has 121 broad-line and 411 Seyfert 2 AGN.
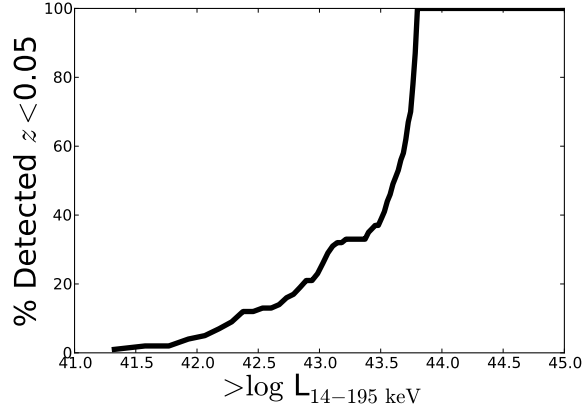
Figure 27. Plot of estimated completeness above a ultra hard X-ray luminosity within the redshift range of this survey (z<0.05) using the median flux sensitivity of the 58 month survey (1.1×10^{-11} erg cm^{-2} s^{-1}; Baumgartner et al. 2011, submitted). This plot assumes the ultra hard X-ray AGN are randomly distributed by volume and uses the distribution of lower redshift sources to estimate those missed at higher redshift. We find that the BAT sources are complete for z< 0.05 in this survey for log $L_{14-195\,\mathrm{keV}} > 43.7$ or $\approx$log $L_{2-10\,\mathrm{keV}} > 43.2$ assuming no intrinsic absorption.

X-ray luminosity. We see that the highest luminosity quartile for BAT luminosity is less complete than the lowest quartile, although this difference is <20%.

In addition, the BAT survey may miss heavily obscured Compton-thick sources that may be identified using methods at other wavelengths. Compton-thick sources are AGN where our line of sight to the source is blocked with obscuring matter that has an optical depth of $\tau > 1$ ($N_{\mathrm{H}} > 1.5 \times 10^{24}$ cm^{-2}). At these optical depths, much of the X-ray emission is reflected and not direct. For Compton-thick sources, the column densities are so high that little to no direct emission escapes below 10 keV. Estimates of the number of Compton-thick sources in the BAT AGN sample have ranged from 3% to 20% (Tueller et al. 2008; Winter et al. 2009; Ajello et al. 2008). A recent analysis of the *INTEGRAL* AGN at 20–40 keV finds that the number of Compton-Thick AGN found by optical and ultra hard X-ray methods is in agreement up to z=0.015 (Malizia et al. 2009).

We independently estimated the number of missing Compton-thick sources by investigating the difference in narrow and broad-line sources by redshift. A plot of average ultra hard X-ray luminosity compared to redshift for narrow-line and broad-line AGN in the BAT survey can be found in Fig. 29. We have also plotted the approximate all-sky limiting flux of the BAT ultra hard X-ray detections for the 58 month catalog. This shows that the BAT survey does have a slight tendency to find narrow-line AGN at closer redshifts than broad-line AGN. The mean redshift is 0.027 for broad-line sources and 0.022 for narrow-line sources. The mean log $L_{14-195\,\mathrm{keV}}$ is 43.56±0.65 for broad-line sources and is 43.37±0.59 for the narrow-line sources.

An additional way to estimate the number of missed absorbed sources is by measuring the percentage of NL BAT AGN by redshift (Fig. 30). We find that the number of narrow-line sources falls at higher redshifts. For z<0.01, 61%
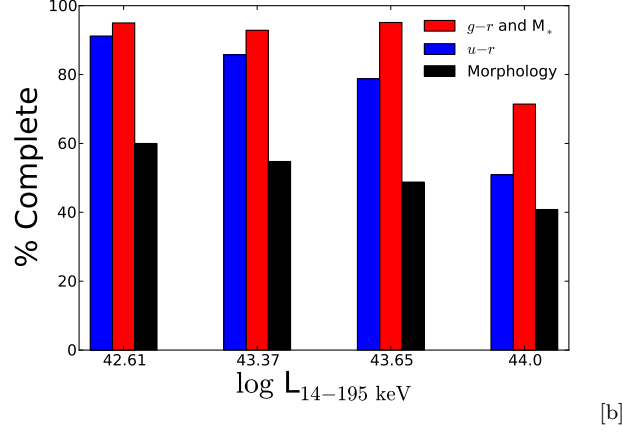
Figure 28. Completeness of various measurements at each quartile of BAT luminosity. Morphology measurements were limited to narrow-line AGN while color measurements exclude systems with very bright AGN. The highest quartile of BAT luminosity is less complete than the lowest quartile, although this difference is <20%.
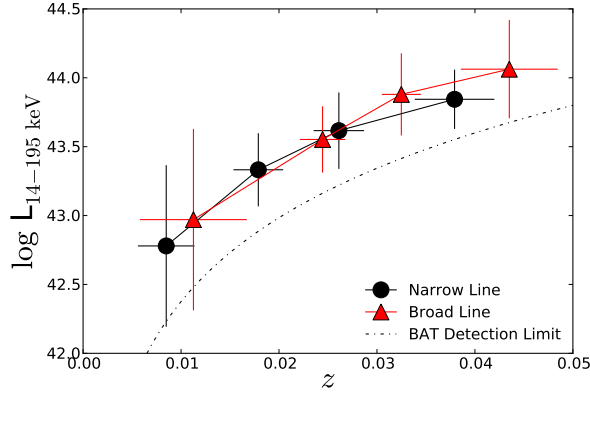
Figure 29. Plot of average ultra hard X-ray luminosity compared to redshift for narrow-line and broad-line AGN in BAT. The error bars indicate standard deviations in each bin. The dashed line shows the approximate flux limit of the BAT survey. This shows that the BAT survey does have a slight tendency to find narrow-line AGN at closer redshifts than broad-line AGN. The mean redshift is 0.027 for broad-line sources and 0.022 for narrow-line sources. The mean $\log L_{14-195\,keV}$ for broad-line sources is 43.56±0.65 and 43.37±0.59.

are NL AGN while at 0.03<z<0.05 only 31% are NL AGN. If we assume that the ratio of 61% narrow-line AGN in the z<0.01 bin is the true value and is constant with redshift, then we will be missing about 50 narrow-line sources at higher redshift or 27% of the entire sample. However, we do not find any statistically significant difference in color between NL and broad-line AGN or between luminous ($\log L_{14-195\,keV}$>43.5) and less luminous sources. We also do not find any statistically significant difference with increasing X-ray column densities. These results suggest that the flux-limited nature of the survey does not strongly influence our overall results.

We can make an additional estimate of the number of missing Compton-thick AGN based on the ratio of NL to broad-line AGN in the SDSS survey. In the redshift range between 0.03 to 0.05, the SDSS has 121 broad-line AGN and 411 NL AGN. For comparison, the BAT survey has 28 broad-line AGN and 17 NL AGN in this range. This suggests that approximately 77% (411/532) are narrow-line, which is greater than the 61% of NL BAT AGN at low redshift, but not outside of the 1 sigma error bars for z<0.02. We may therefore estimate that at a maximum ≈16% AGN are missed as Compton-thick. Unless a large fraction of the missed sources have systematically different colors, morphologies or mass than the detected sources we do not expect a large effect on our results.
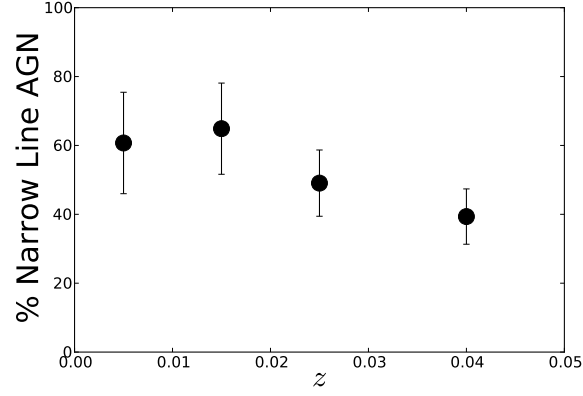
Figure 30. Percent of narrow-line sources in different redshift ranges in the BAT AGN sample. The error bars represent 1σ Poisson statistics. We find that the number of narrow-line sources falls at higher redshifts. For z<0.01, 61% are NL AGN while at 0.03<z<0.05 only 31% are NL AGN. If we assume that the ratio of 61% narrow-line AGN is constant across redshift, we will be missing about 50 narrow-line sources at higher redshift or 27% of the entire sample.

Table 1 Summary of Kitt Peak Observations

Name	Date Obs.	Type [1]	z	Dist. (Mpc)[2]	E(B-V)[3]	Airmass[4]	PSF($''$) [5]
1RXS J045205.0+493248	2008-02-07	Sy1	0.029	125.3	0.72	1.1	1.2
2MASX J00253292+6821442	2008-11-06	Sy2	0.012	51.2	1.04	1.2	2.5
2MASX J04440903+2813003	2008-02-08	Sy2	0.011	48	0.85	1.1	1.0
2MASX J05054575-2351139	2008-11-06	Sy2	0.035	151.9	0.03	1.7	1.5
2MASX J06411806+3249313	2008-02-09	Sy2	0.047	205.8	0.15	1.0	1.0
2MASX J09043699+5536025	2008-02-13	Sy1	0.037	161.4	0.02	1.1	1.2
2MASX J09112999+4528060	2008-02-12	Sy2	0.026	115.5	0.01	1.0	1.4
2MASX J11454045-1827149	2008-02-06	Sy1	0.032	142.7	0.03	1.6	1.4
2MASX J12005792+0648226	2008-02-10	Sy2	0.035	156.1	0.01	1.2	0.9
2MASX J21355399+4728217	2008-11-07	Sy1	0.025	107.6	0.62	1.0	1.0
2MFGC 02280	2008-02-14	G	0.015	64.8	0.77	1.7	2.1
3C 111.0	2008-02-08	Sy1	0.048	210.3	1.65	1.0	0.8
3C 120	2008-11-05	Sy1	0.033	143	0.29	1.3	1.5
Ark 120	2008-02-11	Sy1	0.033	146	0.12	1.2	1.1
ARK 347	2008-02-09	Sy2	0.022	96.9	0.03	1.0	0.8
ARP 102B	2008-02-13	Sy1	0.024	104	0.02	1.3	1.1
CGCG 420-015	2008-02-10	Sy2	0.029	127	0.08	1.2	0.9
ESO 490-IG026	2008-02-10	Sy1.2	0.024	106.8	0.09	2.0	1.3
ESO 506-G027	2008-02-11	Sy2	0.025	107.7	0.07	1.9	1.3
ESO 511-G030	2008-02-09	Sy1	0.022	96.2	0.06	1.9	1.9
FAIRALL 272	2008-02-10	Sy2	0.022	95.4	0.04	1.2	1.0
HB89 0241+622	2008-11-07	Sy1	0.044	192.2	0.72	1.2	1.2
IC 4329A	2008-02-10	Sy1	0.016	68.7	0.05	2.1	1.4
IGR J21277+5656	2008-09-06	Sy1	0.014	62.8	1.3	1.1	1.2
IRAS 04124-0803	2008-02-13	Sy1	0.037	164.9	0.08	1.3	1.4
IRAS 05218-1212	2008-02-13	Sy1	0.049	214.8	0.16	1.4	1.5
IRAS 05589+2828	2008-02-08	Sy1	0.033	143	0.42	1.2	1.0
LEDA 138501	2008-02-11	Sy1	0.049	215.8	0.16	1.1	1.4
LEDA 214543	2008-02-13	Sy2	0.032	138.8	0.11	1.2	1.3
MCG -01-05-047	2008-11-07	Sy2	0.016	72.2	0.02	1.2	1.3
MCG -01-13-025	2008-02-09	Sy1.2	0.015	68	0.03	1.3	1.2
MCG -01-24-012	2008-02-06	Sy2	0.019	84.2	0.03	1.3	1.7
MCG -01-40-001	2008-02-12	Sy2	0.022	97.6	0.08	1.3	2.1
MCG -02-12-050	2008-02-10	Sy2	0.036	157.9	0.07	1.4	0.9
MCG -03-34-064	2008-02-06	Sy1.8	0.016	70.8	0.07	1.5	1.4
MCG -05-14-012	2008-11-06	Sy2	0.009	42.2	0.12	1.9	1.5
MCG -05-23-016	2008-02-11	Sy2	0.008	36.1	0.10	2.2	1.4
MCG +04-22-042	2008-02-12	Sy1.2	0.032	141.5	0.04	1.0	1.6
MCG +04-48-002	2008-09-08	Sy2	0.013	59.3	0.44	1.1	1.1
MCG +08-11-011	2008-11-04	Sy1.5	0.020	87.9	0.21	1.0	0.8
Mrk 10	2008-02-09	Sy1.2	0.029	126.4	0.04	1.2	1.1
Mrk 1018	2008-09-06	Sy1.5	0.042	186.1	0.12	1.2	1.0
Mrk 18	2008-02-09	Sy1	0.011	47.2	0.04	1.2	1.0
Mrk 279	2008-02-07	Sy1.5	0.030	131.7	0.01	1.2	1.3
Mrk 335	2008-11-07	Sy1.2	0.025	109.5	0.02	1.0	1.6
Mrk 348	2008-11-07	Sy2	0.015	64.7	0.06	1.0	1.7
Mrk 352	2008-11-07	Sy1	0.014	63.7	0.06	1.1	1.6
Mrk 417	2008-02-08	Sy2	0.032	142.1	0.02	1.0	0.9
Mrk 509	2008-09-05	Sy1.2	0.034	149.2	0.05	1.5	1.4
Mrk 520	2008-11-04	Sy1.9	0.026	114.7	0.05	1.0	1.0
Mrk 590	2008-02-12	Sy1.2	0.026	113.7	0.03	1.3	1.7
Mrk 79	2008-11-07	Sy1.2	0.022	95.4	0.07	1.0	1.2
Mrk 915	2008-09-05	Sy1	0.024	103.7	0.06	1.4	1.6
NGC 1142	2008-02-13	Sy2	0.028	124.6	0.07	1.2	1.4
NGC 1275	2008-02-12	Sy2	0.017	75.2	0.03	1.2	1.5
NGC 2110	2008-02-06	Sy2	0.007	33.1	0.37	1.6	1.8
NGC 2992	2008-11-06	Sy2	0.007	30.5	0.06	1.8	1.3
NGC 3081	2008-02-10	Sy2	0.007	32.5	0.05	1.7	1.0
NGC 3227	2008-02-08	Sy1.5	0.003	20.9	0.02	1.0	0.8
NGC 3281	2008-02-11	Sy2	0.010	45.4	0.16	2.6	1.4
NGC 3516	2008-02-07	Sy1.5	0.008	38.9	0.04	1.3	1.6
NGC 4102	2008-02-12	LINER	0.002	21	0.02	1.0	2.1
NGC 4593	2008-02-08	Sy1.9	0.009	44	0.02	1.2	1.4
NGC 5728	2008-02-08	Sy2	0.009	29.1	0.10	1.5	1.4
NGC 5995	2008-02-11	Sy2	0.025	108.5	0.15	1.4	1.8
NGC 6240	2008-02-14	Sy2	0.024	105.4	0.07	1.3	2.0
NGC 6814	2008-09-05	Sy1.5	0.005	22.8	0.18	1.4	1.2
NGC 7314	2008-11-06	Sy1.9	0.004	19	0.02	1.9	2.0
NGC 7319	2008-09-08	Sy2	0.022	95.3	0.07	1.1	1.0
NGC 7469	2008-11-05	Sy1.2	0.016	69.8	0.06	1.3	2.5
NGC 7679	2008-09-06	Sy1	0.017	73.4	0.06	1.1	1.4
NGC 7682	2008-11-07	Sy2	0.017	73.1	0.06	1.1	1.3
NGC 788	2008-11-06	Sy2	0.013	58	0.02	1.3	1.2
NGC 931	2008-02-10	Sy1.5	0.016	71.2	0.09	1.1	0.9
NGC 973	2008-11-05	Sy2	0.016	69.2	0.09	1.2	1.6
RX J2044.0+2833	2008-11-06	Sy1	0.05	219.4	0.03	1.2	1.7

Continued on Next Page. . .

TABLE 1 – Continued

Name	Date Obs.	Type [1]	z	Dist. (Mpc)[2]	E(B-V)[3]	Airmass[4]	PSF($''$) [5]
SBS 1301+540	2008-02-12	Sy1	0.029	129.2	0.02	1.0	1.5
UGC 02724	2008-11-07	Sy2	0.047	209	0.20	1.1	1.3
UGC 03142	2008-02-09	Sy1	0.021	93	0.74	1.0	1.1
UGC 03601	2008-02-09	Sy1.5	0.017	73.3	0.08	1.0	0.9
UGC 12282	2008-09-07	Sy1.9	0.016	72.7	0.14	1.0	1.3
UGC 12741	2008-09-08	G	0.017	74.7	0.10	1.1	2.4

[0] This table is also available in its entirety as a supplementary file in ASCII format.

[1] AGN type and host galaxy type from Tueller et al. (2008). For AGN types, optical identifications are listed, where available. Where G is indicated, there are no optical emission lines indicative of the presence of an AGN and the optical spectrum looks like a galaxy spectrum.

[2] We used the mean of the redshift independent distance in Mpc from NED when available. Otherwise, we adopted the following cosmological parameters to determine distances: $\Omega_m = 0.27$, $\Omega_\Lambda = 0.73$, and $H_0 = 71$ km s^{-1} Mpc^{-1}.

[3] Milky Way reddening values, E(B-V), from *IRAS* and *COBE/DIRBE*.

[4] Median airmass of all five filter observations.

[5] Gaussian FWHM of r band image.

Table 2 Summary of SDSS Observations

Name	Date Obs.	Type [1]	z	Dist. (Mpc)[2]	E(B-V)[3]	Airmass[4]	PSF($''$) [5]
2MASX J01064523+0638015	2005-09-28	Sy2	0.041	178.7	0.05	1.1	1.0
2MASX J03305218+0538253	2004-12-14	Sy1	0.046	201.3	0.37	1.1	1.7
2MASX J03534246+3714077	2003-01-28	Sy2	0.018	78.4	0.53	1.0	0.9
2MASX J07595347+2323241	2003-01-25	Sy2	0.029	128	0.05	1.4	1.4
2MASX J16174158+0607100	2003-04-25	Sy2	0.037	164.8	0.08	1.1	0.9
ARP 151	2002-04-01	Sy1	0.021	90.5	0.02	1.2	1.5
CGCG 031-072	2002-03-05	Sy1	0.033	143.2	0.03	1.2	1.8
CGCG 046-033	2001-04-16	Sy1.5	0.034	148.7	0.03	1.2	1.2
CGCG 102-048	2005-05-09	Sy1.9	0.026	116	0.03	1.1	1.2
CGCG 122-055	2004-12-13	Sy1	0.021	91.8	0.03	1.0	1.1
CGCG 198-020	2006-05-24	Sy1	0.026	112	0.04	1.2	1.6
CGCG 300-062	2001-09-20	Sy2	0.032	143	0.05	1.3	0.9
CGCG 312-012	2003-10-24	Sy2	0.025	110.3	0.04	1.3	1.5
CGCG 319-007	2004-06-15	Sy1.9	0.044	192.2	0.04	1.2	1.3
CGCG 427-028	2006-05-27	G	0.030	131	0.20	1.3	1.7
IC 0486	2002-01-14	Sy1.8	0.027	117.5	0.03	1.1	1.1
IC 0751	2003-04-01	Sy2	0.030	134.1	0.03	1.2	1.4
IC 2461	2002-11-07	Sy2	0.007	72.9	0.01	1.1	1.4
IC 2515	2003-03-07	Sy2	0.019	82.7	0.02	1.0	1.1
KAZ 320	2006-09-18	Sy1	0.034	149.6	0.15	1.6	1.6
KUG 1141+371	2004-01-31	Sy1	0.038	165.5	0.02	1.0	1.4
KUG 1208+386	2004-01-31	Sy1	0.022	98	0.03	1.0	1.6
LEDA 170194	2006-01-31	Sy2	0.036	159.4	0.04	1.4	1.4
M106	2003-03-06	LINER	0.001	7.5	0.01	1.3	1.3
MCG -02-08-014	1999-10-14	G	0.016	71.7	0.05	1.8	1.8
MCG +01-57-016	2005-09-26	Sy1.8	0.024	107.5	0.12	1.1	1.2
MCG +02-21-013	2005-03-10	Sy2	0.034	149.3	0.03	1.0	1.4
MCG +04-06-043	2005-11-04	Sy1	0.033	144.5	0.21	1.2	1.3
MCG +05-28-032	2004-12-15	LINER	0.023	99	0.02	1.1	1.3
MCG +06-24-008	2004-02-17	Sy2	0.025	111.5	0.02	1.0	1.2
MCG +06-49-019	2006-09-16	Sy2	0.021	91.6	0.17	1.0	1.3
MCG +11-11-032	2003-11-20	Sy2	0.036	156.3	0.15	1.3	1.3
MCG+10-17-061	2001-04-15	G	0.009	42.3	0.02	1.1	1.5
MRK 1044	1999-10-14	Sy1.8	0.016	70.4	0.05	1.5	1.5
Mrk 110	2001-02-22	Sy1	0.035	153.6	0.01	1.2	1.2
Mrk 1210	2003-01-28	Sy1	0.013	57.6	0.02	1.0	1.0
Mrk 1392	2001-03-19	Sy1	0.036	157.3	0.04	1.5	1.5
Mrk 1469	2002-02-08	Sy1	0.030	134.1	0.03	1.0	1.3
Mrk 198	2003-03-06	Sy2	0.024	105.8	0.01	1.3	1.3
Mrk 268	2004-04-25	Sy2	0.039	173.6	0.02	1.1	1.3
Mrk 290	2001-03-23	Sy1	0.029	128.1	0.01	1.5	1.5
Mrk 463E	2005-05-09	Sy2	0.050	221	0.04	1.1	1.0
Mrk 464	2004-01-28	Sy1.5	0.050	222.8	0.02	1.0	1.0
Mrk 477	2002-05-09	Sy2	0.037	164	0.01	1.1	1.7
Mrk 50	2000-05-05	Sy1	0.023	99.7	0.01	1.3	1.3
Mrk 595	2005-10-12	Sy1.5	0.026	116.4	0.17	1.2	1.1
Mrk 704	2005-03-12	Sy1.5	0.029	126.3	0.02	0.9	0.9
Mrk 705	2006-01-31	Sy1.2	0.028	120.8	0.04	1.2	1.2
Mrk 728	2003-03-23	Sy1	0.035	154.7	0.03	1.3	1.5
Mrk 732	2002-12-11	Sy1.8	0.029	126.3	0.03	1.2	1.5
Mrk 739E	2005-03-10	Sy1	0.029	128.4	0.03	1.0	1.5
Mrk 766	2004-12-15	Sy1.5	0.012	54	0.01	1.2	1.2
Mrk 78	2004-12-13	Sy2	0.037	158.1	0.05	1.2	1.2
Mrk 817	2001-05-18	Sy1.5	0.031	135.2	0.00	1.7	1.7
Mrk 841	2003-04-25	Sy1	0.036	158.2	0.02	1.4	1.4
Mrk 926	2000-09-03	Sy1.5	0.047	206.5	0.04	1.4	1.4
NGC 0835	2000-09-26	Sy2	0.013	56.3	0.03	1.3	1.5
NGC 1012	2005-12-06	G	0.003	16.2	0.21	1.2	1.3
NGC 1052	1999-10-14	Sy2	0.004	19.6	0.02	1.6	1.6
NGC 1194	2002-09-05	Sy1.8	0.013	56.9	0.07	1.4	1.4
NGC 235A	2006-09-17	Sy2	0.022	95.5	0.01	1.7	1.5
NGC 2885	2004-12-13	Sy1	0.026	112	0.04	1.0	1.1
NGC 3079	2001-04-15	Sy2	0.003	19.3	0.01	1.4	1.4
NGC 3718	2002-01-13	LINER	0.003	17	0.01	1.5	1.5
NGC 3786	2004-05-14	Sy1.8	0.008	41.6	0.03	1.1	1.3
NGC 4051	2003-03-26	Sy1.5	0.002	14.5	0.01	1.2	1.2
NGC 4138	2003-04-25	Sy1.9	0.002	15.6	0.01	1.2	1.2
NGC 4235	2003-04-01	Sy1	0.007	35.1	0.01	1.0	1.0
NGC 4388	2003-03-23	Sy2	0.008	18.25	0.03	1.4	1.4
NGC 4395	2004-04-25	Sy1.8	0.001	4.11	0.01	1.5	1.5
NGC 452	2004-08-26	G	0.016	70.8	0.09	1.0	1.7
NGC 4686	2002-04-01	G	0.016	71.7	0.01	1.3	1.3
NGC 4992	2003-03-31	G	0.025	108.5	0.02	1.3	1.3
NGC 5106	2003-04-28	LINER	0.031	138.3	0.04	1.1	1.1
NGC 513	2004-09-15	Sy2	0.019	83.9	0.06	1.4	1.4
NGC 5231	2000-05-04	Sy2	0.021	93.5	0.03	1.3	1.2

Continued on Next Page...

TABLE 2 – Continued

Name	Date Obs.	Type [1]	z	Dist. (Mpc)[2]	E(B-V)[3]	Airmass[4]	PSF($''$) [5]
NGC 5252	2001-03-19	LINER	0.022	95.5	0.03	1.4	1.4
NGC 5273	2004-03-17	Sy1.9	0.003	17.7	0.01	1.0	1.0
NGC 5290	2003-04-25	Sy2	0.008	35.7	0.01	1.0	1.6
NGC 5506	2001-05-24	Sy1.9	0.006	28.7	0.05	1.3	1.3
NGC 5548	2004-06-12	Sy1.5	0.016	71.4	0.01	1.3	1.3
NGC 5610	2004-06-13	Sy2	0.016	72.3	0.03	1.0	1.4
NGC 5674	2001-06-16	Sy1.9	0.024	107.3	0.05	1.1	1.4
NGC 5683	2002-05-08	Sy1	0.036	157.3	0.04	1.2	1.5
NGC 5899	2003-04-29	Sy2	0.008	43.9	0.03	1.3	1.3
NGC 5940	2003-04-27	Sy1	0.034	147.4	0.06	1.3	1.2
NGC 7603	2001-10-15	Sy1.5	0.029	126.6	0.04	1.0	1.0
NGC 985	1999-10-14	Sy1	0.043	187.7	0.09	1.5	1.5
SDSS J104326.47+110524.2	2002-12-14	Sy1	0.047	208.4	0.04	1.0	1.3
UGC 03995A	2001-12-18	Sy2	0.015	68	0.04	1.0	1.6
UGC 05881	2005-01-17	Sy2	0.020	88.1	0.04	1.0	1.0
UGC 06527 NED03	2001-12-20	Sy2	0.026	113.9	0.01	1.1	1.1
UGC 07064	2004-12-15	Sy1.9	0.025	107.6	0.02	1.1	1.1
UGC 08327 NED02	2003-03-24	Sy2	0.036	158.8	0.02	1.2	1.5
UGC 11185 NED02	2005-06-08	Sy2	0.041	174.2	0.07	1.1	1.1
UM 614	2000-05-05	Sy1	0.032	142.3	0.02	1.2	1.2
VII Zw 073	2004-10-15	Sy2	0.041	180.1	0.12	1.1	1.2

[0] This table is also available in its entirety as a supplementary file in ASCII format.
[1] AGN type and host galaxy type from Tueller et al. (2008). For AGN types, optical identifications are listed, where available. Where G is indicated, there are no optical emission lines indicative of the presence of an AGN and the optical spectrum looks like a galaxy spectrum.

[2] We used the mean of the redshift independent distance in Mpc from NED when available. Otherwise, we adopted the following cosmological parameters to determine distances: $\Omega_m = 0.27$, $\Omega_\Lambda = 0.73$, and $H_0 = 71$ km s^{-1} Mpc^{-1}.
[3] Milky Way reddening values, E(B-V), from *IRAS* and *COBE/DIRBE*.
[4] Median airmass of all five filter observations.
[5] Gaussian FWHM of r band image.

<div align="center">

Table 3
Observing Summary–Filter Limiting Magnitudes and PSF

</div>

	u	g	r	i	z
SDSS [mag][1]	22.3	23.3	22.9	22.3	20.7
Kitt Peak [mag]	24.2	24.8	24.4	23.7	22.0
SDSS ($''$)[2]	1.36±0.22	1.30±0.19	1.17±0.17	1.14±0.18	1.15±0.18
Kitt Peak ($''$)	1.67±0.76	1.56±0.47	1.46±0.41	1.44±0.59	1.42±0.48

[1] Detection based on overlapping fields in SDSS and Kitt Peak sample with at least
5 pixels above signal-to-noise ratio>3.
[2] PSF function was calculated using the FWHM of a single gaussian fit to the 10
brightest unsaturated stars.

<div align="center">

Table 4 Summary of Photometry and Derived Properties

</div>

Galaxy	u[1] mag	g mag	r mag	i mag	z mag	log $\mathbf{M}_*$[2] $M_\odot$	$\mathbf{PS}_r$[3] %	$\mathbf{E}(g-r)$[4] mag	$\mathbf{E}(g-r)$ Incl. [5] mag	u[6] Contam.	$griz$[7] Contam.
2MASX J00253292+6821442	$\cdots$	12.86	12.14	11.85	11.9	10.05	3.59	0.03	$\cdots$		
2MASX J01064523+0638015	16.9	15.54	14.76	14.27	14.15	10.4	2.75	0.14	0.01		
2MASX J03534246+3714077	15.84	13.99	13.5	13.31	13.18	9.9	1.67	0.21	$\cdots$		
2MASX J04440903+2813003	$\cdots$	12.68	11.8	11.4	11.3	10.41	2.51	0.24	$\cdots$		
2MASX J05054575-2351139	17.31	16.11	15.44	15.12	15.36	9.13	12.7	0.03	$\cdots$		
2MASX J06411806+3249313	17.9	16.56	15.95	15.56	15.25	9.94	3.25	0.44	$\cdots$		
2MASX J07595347+2323241	15.44	14.11	13.41	13.02	12.65	10.57	1.59	0.34	0.04		
2MASX J09043699+5536025	17.61	16.25	15.81	15.31	15.16	9.76	29.1	0.62	$\cdots$	Y	
2MASX J09112999+4528060	17.57	15.98	15.19	14.77	14.54	9.76	2.16	0.27	$\cdots$		
2MASX J12005792+0648226	15.72	14.68	13.91	13.49	13.34	10.58	1.28	0.17	$\cdots$		
2MASX J16174158+0607100	18.06	16.24	15.37	14.92	14.60	10.14	0.99	0.31	0.08		
2MASX J21355399+4728217	16.32	14.84	14.12	13.82	14.25	9.41	21.4	0	0.1	Y	
2MFGC 02280	$\cdots$	14.1	13.26	12.84	12.64	10.13	3.69	0.27	0.09		
ARK 347	16.29	14.5	13.75	13.36	13.10	10.3	2.83	0.34	$\cdots$		
ARP 102B	17.31	15.05	14.06	13.65	13.37	10.25	8.47	0.14	$\cdots$		
ARP 151	17.54	16.01	15.08	14.69	14.51	9.71	17.0	0.21	$\cdots$		
CGCG 031-072	16.94	15.30	14.59	14.19	14.00	10.27	15.1	0.17	$\cdots$		
CGCG 046-033	16.05	14.90	14.32	14.00	13.96	10.18	9.90	0.03	0.02		
CGCG 102-048	16.81	15.21	14.38	13.91	13.6	10.31	2.46	0.38	0.06		
CGCG 122-055	16.99	15.01	14.32	13.96	13.65	9.94	15.4	0.41	$\cdots$		
CGCG 198-020	16.34	14.49	13.81	13.39	13.23	10.38	5.24	0.31	$\cdots$		
CGCG 300-062	16.57	15.17	14.56	14.20	14.31	9.9	3.28	0	0.02		
CGCG 312-012	16.35	14.78	13.97	13.59	13.34	10.3	1.94	0.07	$\cdots$		
CGCG 319-007	18.11	15.09	14.35	13.95	13.75	10.63	4.20	1.03	$\cdots$		
CGCG 420-015	15.75	14.13	13.43	13.04	12.71	10.63	3.37	0.34	$\cdots$		
CGCG 427-028	16.42	14.77	13.93	13.49	13.25	10.51	3.69	0.21	$\cdots$		
ESO 490-IG026	15.52	13.45	12.74	12.27	12.32	10.67	8.95	0.31	$\cdots$		
ESO 506-G027	18	14.78	14.12	13.14	14.06	9.84	2.18	0.62	0.07		
ESO 511-G030	14.20	12.72	11.93	11.35	11.11	11.09	7.31	0.51	0.02		
FAIRALL 272	15.53	14.67	13.96	13.57	13.39	10.08	1.58	0.21	$\cdots$		
IC 0486	15.34	13.91	13.21	12.88	12.64	10.61	2.35	0	0.03		
IC 0751	15.44	14.36	13.71	13.31	13.07	10.48	4.65	0.21	0.08		
IC 2461	16.79	14.03	13.36	12.93	12.60	9.54	0.53	0.72	0.09		
IC 2515	15.69	14.54	13.85	13.40	13.15	10.04	3.73	0.38	0.09		
IC 4329A	15.35	13.24	12.40	11.83	11.89	10.53	25.8	0.27	0.08	Y	
KUG 1141+371	$\cdots$	15.69	14.94	14.54	14.46	10.19	7.11	0.14	$\cdots$		
KUG 1208+386	$\cdots$	14.97	14.31	13.88	13.59	10.02	23.3	0.44	$\cdots$	Y	
LEDA 170194	15.05	14.35	13.74	13.40	13.21	10.59	3.01	0.92	0.01		
LEDA 214543	17.6	15.29	14.43	14.05	13.75	10.35	6.02	0.62	$\cdots$		
M106	10.81	8.74	8.11	7.775	7.875	9.95	0.45	0.21	0.06		
MCG -01-05-047	14.89	13.45	12.68	12.2	11.95	10.5	0.02	0.44	0.12		
MCG -01-13-025	15.23	13.80	13.05	12.68	12.42	10.23	5.39	0.17	$\cdots$		
MCG -01-24-012	16.22	14.33	13.66	13.27	13.12	10.16	3.83	0.31	0.04		
MCG -01-40-001	14.63	13.21	12.56	12.11	12.09	10.66	2.53	0.14	0.06		
MCG -02-08-014	17	14.69	13.9	13.42	13.12	10.01	4.74	0.65	0.11		
MCG -02-12-050	15.32	14.01	13.39	13.02	12.87	10.73	8.09	0.24	$\cdots$		
MCG -03-34-064	15.81	13.65	12.79	12.37	12.2	10.43	13.1	0.44	$\cdots$		
MCG -05-14-012	15.01	13.91	13.28	12.95	12.76	9.66	9.63	0.07	$\cdots$		
MCG -05-23-016	15.73	14.01	13.47	12.72	12.85	9.56	1.92	0.38	$\cdots$		
MCG +01-57-016	15.88	14.17	13.58	13.30	13.23	10.26	16.7	0.14	0.01		
MCG +02-21-013	16.11	14.4	13.68	13.24	13.07	10.68	0.73	0.21	$\cdots$		
MCG +04-06-043	15.53	14.96	14.23	14.07	13.80	10.3	28.3	0	0.01	Y	
MCG +04-22-042	16.62	14.78	14.06	13.61	13.51	10.49	21.4	0.31	0.03	Y	
MCG +04-48-002	15.08	13.45	12.7	12.41	12.22	10.2	1.11	0.14	$\cdots$		

Continued on Next Page. . .

TABLE 4 – Continued

Galaxy	u[1] mag	g mag	r mag	i mag	z mag	log $\mathbf{M}_*$[2] M$_\odot$	$\mathbf{PS}_r$[3] %	$\mathbf{E}(g-r)$[4] mag	$\mathbf{E}(g-r)$ Incl. [5] mag	u[6] Contam.	$griz$[7] Contam.
MCG +05-28-032	16.52	15.04	14.23	13.74	13.44	10.14	1.07	0.48	0.04		
MCG +06-24-008	15.7	14.64	13.97	13.56	13.28	10.23	1.83	0.27	0.08		
MCG +06-49-019	15.37	13.58	12.82	12.46	12.30	10.56	4.52	0.31	0.03		
MCG +08-11-011	14.41	12.78	12.04	11.58	11.42	10.91	21.2	0.34	0.02	Y	
MCG +11-11-032	19.09	15.8	14.89	14.39	14.06	10.33	4.13	1.03	0.05		
MCG+10-17-061	14.98	13.43	12.86	12.54	12.33	9.8	2.48	0.21	$\cdots$		
Mrk 10	15.30	13.62	12.97	12.57	12.49	10.73	4.92	0.21	0.05		
Mrk 1018	16.59	14.45	13.65	13.28	13.06	10.92	21.6	0.21	$\cdots$	Y	
Mrk 110	17.19	15.83	15.20	14.89	14.80	9.9	24.6	0	$\cdots$	Y	
Mrk 1210	14.94	13.97	13.32	13.03	12.82	9.89	7.31	0.31	$\cdots$		
Mrk 1392	16.07	14.41	13.80	13.39	13.05	10.64	19.5	0.68	0.04		
Mrk 1469	16.88	15.48	14.64	14.22	13.95	10.22	8.79	0.24	$\cdots$		
Mrk 18	15.19	14.07	13.44	13.16	12.87	9.57	8.95	0.07	$\cdots$		
Mrk 198	16.03	14.64	14.02	13.69	13.45	10.12	2.83	0.14	0.01		
Mrk 268	15.88	14.58	13.88	13.49	13.19	10.64	5.70	0.17	$\cdots$		
Mrk 279	15.24	14.48	13.74	13.35	13.16	10.49	26.7	0.31	$\cdots$	Y	
Mrk 348	14.8	13.29	12.59	12.1	12.1	10.33	2.33	0.14	0		
Mrk 352	$\cdots$	14.94	14.27	13.92	13.73	9.65	17.7	0.14	$\cdots$		
Mrk 417	16.87	15.32	14.65	14.27	14.01	10.2	3.13	0.31	$\cdots$		
Mrk 463E	15.58	14.36	14.04	13.65	13.55	10.61	5.24	0.44	$\cdots$		
Mrk 464	$\cdots$	16.92	16.44	16.15	15.94	9.67	33.4	0.31	$\cdots$	Y	
Mrk 477	15.97	14.78	14.73	14.45	14.34	9.87	19.2	0.24	$\cdots$		
Mrk 50	17.07	15.41	14.69	14.32	14.01	9.9	11.3	0.27	$\cdots$		
Mrk 520	15.19	14.14	13.52	13.18	13.00	10.4	4.92	0.14	0.03		
Mrk 590	15.76	13.29	12.66	12.20	12.13	10.84	3.40	0.58	$\cdots$		
Mrk 595	16.07	14.75	14.07	13.72	13.50	10.3	19.2	0.14	$\cdots$		
Mrk 705	15.17	14.85	14.22	13.86	13.57	10.18	22.4	0.41	$\cdots$	Y	
Mrk 728	17.99	15.87	15.19	14.79	14.42	10.09	16.2	0.58	$\cdots$		
Mrk 732	15.15	13.89	13.33	13.03	12.85	10.48	7.37	0.17	$\cdots$		
Mrk 739E	15.17	14.12	13.86	13.16	12.88	10.47	6.79	0.68	$\cdots$		
Mrk 766	14.91	13.50	12.95	12.59	12.37	10.02	14.9	0.31	0.01		
Mrk 78	16.56	14.73	14.28	13.87	13.68	10.42	0.11	0.44	$\cdots$		
Mrk 79	15.02	13.52	12.81	12.45	12.14	10.57	21.6	0.34	0.01	Y	
Mrk 817	16.38	14.61	13.92	13.61	13.47	10.41	34.3	0.07	0.01	Y	
Mrk 915	15.63	14.17	13.43	13.09	12.86	10.43	6.42	0	0.06		
Mrk 926	16.24	14.66	13.78	13.45	13.37	10.82	13.0	0.14	0.01		
NGC 0835	13.91	12.62	11.94	11.56	11.31	10.48	1.51	0.21	$\cdots$		
NGC 1012	12.78	12.16	11.72	11.46	11.24	9.18	0.11	0.79	0.04		
NGC 1052	12.82	11.14	10.35	9.924	9.680	10.35	0.83	0.27	$\cdots$		
NGC 1142	14.08	13.13	12.44	12.08	11.76	10.93	3.53	1.03	$\cdots$		
NGC 1194	15.24	13.19	12.45	12.00	11.93	10.32	1.23	0.38	$\cdots$		
NGC 1275	12.8	11.7	11.03	10.65	10.71	10.94	3.25	0	$\cdots$		
NGC 2110	13.89	11.25	10.43	10.01	9.94	10.63	1.45	0.68	$\cdots$		
NGC 235A	15	13.71	13.02	12.64	12.40	10.49	7.11	0.21	$\cdots$		
NGC 2885	15.85	14.26	13.47	13.03	12.80	10.56	2.46	0.31	0.02		
NGC 2992	13.59	12.08	11.37	10.95	10.71	10.31	0.00	0.27	$\cdots$		
NGC 3079	11.91	10.97	10.34	9.926	9.703	9.98	0.09	1.03	0.11		
NGC 3081	13.84	12.19	11.51	11.07	10.85	10.31	0.32	0.34	0.02		
NGC 3227	13.49	11.60	10.76	10.18	9.965	9.98	7.11	0.51	$\cdots$		
NGC 3281	14.59	12.83	12.41	11.76	11.24	10.24	0.20	0.82	0.04		
NGC 3516	14.23	12.22	11.39	10.93	10.77	10.46	10.3	0.44	$\cdots$		
NGC 3718	12.87	11.11	10.41	9.990	9.759	9.98	0.89	0.34	0.05		
NGC 3786	13.85	12.86	12.20	11.83	11.40	10.01	6.19	1.03	$\cdots$		
NGC 4051	12.04	10.78	10.26	9.996	9.847	9.44	4.09	0	0.02		
NGC 4102	13.13	11.45	10.73	10.32	9.990	9.68	2.07	0.38	0.05		
NGC 4138	13.35	11.68	10.97	10.58	10.40	9.61	0.77	0.17	0.03		
NGC 4235	14.12	12.12	11.36	10.93	10.66	10.36	1.20	0.44	0.09		
NGC 4388	12.64	11.33	10.72	10.35	10.04	10.53	0.03	0.31	0.1		
NGC 4395	11.40	10.52	10.22	10.08	10.11	8.28	0.39	0.03	0.01		
NGC 452	14.75	13.38	12.59	12.15	11.89	10.48	3.25	0.27	0.08		
NGC 4593	14.48	11.48	10.74	10.24	10.09	10.75	2.35	0.79	0.02		
NGC 4686	14.59	13.01	12.18	11.75	11.45	10.68	0.81	0.24	$\cdots$		
NGC 4992	15.51	13.9	13.17	12.70	12.53	10.64	2.12	0.27	$\cdots$		
NGC 5106	15.81	14.21	13.53	13.13	12.83	10.59	3.22	0.34	$\cdots$		
NGC 513	14.74	13.41	12.74	12.41	12.13	10.44	4.83	0.1	$\cdots$		
NGC 5231	15.33	13.74	13.03	12.65	12.42	10.51	3.94	0.24	0.04		
NGC 5252	$\cdots$	13.47	12.73	12.35	11.95	10.59	1.67	0.24	$\cdots$		
NGC 5273	14.72	12.10	11.38	11.03	10.77	9.64	1.75	1.03	$\cdots$		
NGC 5290	13.41	12.42	11.65	11.18	10.96	10.23	1.24	0.31	0.08		
NGC 5506	15.21	12.39	11.66	11.24	10.91	10.02	2.83	0.75	$\cdots$		
NGC 5548	14.49	13.08	12.48	12.09	11.95	10.46	6.60	0.24	0.01		
NGC 5610	14.71	13.29	12.71	12.39	12.09	10.28	1.58	0.24	0.07		
NGC 5674	14.10	13.13	12.70	12.35	12.15	10.57	3.80	0.51	0		
NGC 5683	16.66	15.44	14.73	14.44	14.25	10.22	23.5	0.07	$\cdots$	Y	
NGC 5728	13.69	11.44	10.73	10.27	10.05	10.78	0.60	0.58	0.03		
NGC 5899	13.56	12.18	11.47	11.11	10.84	10.28	2.37	0.1	0.05		

Continued on Next Page...

TABLE 4 – Continued

Galaxy	u^1 mag	g mag	r mag	i mag	z mag	log M_*[2] $M_\odot$	PS_r[3] %	$E(g-r)$[4] mag	$E(g-r)$ Incl. [5] mag	u[6] Contam.	$griz$[7] Contam.
NGC 5940	16.23	13.91	13.47	13.14	13.16	10.47	11.0	0.38	0		
NGC 5995	16.62	15.42	14.67	14.38	14.21	9.89	2.44	0	$\cdots$		
NGC 6240	15.32	13.11	12.21	11.66	11.54	11.03	1.88	0.55	$\cdots$		
NGC 6814	12.36	11.05	10.41	10.01	9.840	10.3	3.10	0.27	0		
NGC 7314	12.28	11.21	10.61	10.28	10.10	10.06	0.38	0.1	0.05		
NGC 7319	14.58	13.5	12.75	12.37	12.16	10.61	1.75	0.17	$\cdots$		
NGC 7469	13.72	12.95	12.39	11.86	11.58	10.49	16.2	1.03	$\cdots$		
NGC 7603	13.98	13.28	12.66	12.19	11.82	10.94	29.3	0.75	$\cdots$	Y	
NGC 7679	13.97	12.94	12.50	12.31	12.16	10.17	5.54	0.03	0.03		
NGC 7682	14.95	13.29	12.57	12.16	11.91	10.53	1.21	0.27	0.01		
NGC 788	14.28	12.51	11.75	11.3	11	10.68	1.70	0.44	0.02		
NGC 931	14.63	13.08	12.51	11.82	11.55	10.6	27.0	0.82	$\cdots$	Y	
NGC 973	14.81	12.95	12.06	11.44	10.74	10.84	0.65	1.03	0.12		
NGC 985	15.74	14.07	13.62	13.19	13.22	10.71	29.9	0.17	$\cdots$	Y	
SBS 1301+540	17.50	15.87	15.30	14.88	14.81	9.79	14.5	0.17	0.05		
UGC 02724	16.77	15.47	15.02	14.63	14.63	10.04	3.53	0.07	0.03		
UGC 03142	14.58	12.52	12.29	12.03	12.09	10.21	7.65	0.17	0.02		
UGC 03601	16.01	14.37	13.67	13.32	13.10	10.04	6.85	0.14	$\cdots$		
UGC 03995A	13.2	12.69	12.06	11.70	11.40	10.57	2.67	0.96	0.05		
UGC 05881	15.66	14.35	13.62	13.26	13.05	10.22	2.75	0.07	0.06		
UGC 06527 NED03	16.21	14.68	14.03	13.69	13.48	10.22	1.90	0.14	$\cdots$		
UGC 07064	14.89	13.7	13.11	12.72	12.50	10.54	5.10	0.34	0.01		
UGC 08327 NED02	16.79	14.88	14.09	13.73	13.47	10.55	5.59	0.34	$\cdots$		
UGC 11185 NED02	16.34	15.24	14.6	14.12	13.85	10.41	2.2	0.72	$\cdots$		
UGC 12282	14.67	13.02	12.11	11.52	11.33	10.78	1.06	0.44	$\cdots$		
UGC 12741	15.48	14.14	13.49	13.13	12.96	10.08	1.16	0.07	0.08		
UM 614	15.65	15.83	15.15	14.82	14.67	9.99	28.3	0.07	$\cdots$	Y	
VII Zw 073	16.19	15.1	14.58	14.23	14.08	10.33	2.35	0.17	0.01		
1RXS J045205.0+493248	14.55	14.06	13.69	13.44	13.50	10.1	39.8	$\cdots$	$\cdots$	Y	Y
2MASX J03305218+0538253	15.65	15.46	15.44	15.04	15.15	10.02	58.6	$\cdots$	$\cdots$	Y	Y
2MASX J11454045-1827149	15.43	15.00	15.28	14.31	14.18	10.04	76.5	$\cdots$	$\cdots$	Y	Y
3C 111.0	$\cdots$	15.57	14.26	13.96	14.36	10.03	80.1	$\cdots$	$\cdots$	Y	Y
3C 120	15.23	14.10	13.55	13.19	13.21	10.41	48.3	$\cdots$	$\cdots$	Y	Y
Ark 120	13.99	13.59	13.21	13.04	12.84	10.72	52.4	$\cdots$	$\cdots$	Y	Y
HB89 0241+622	16.79	15.94	15.11	14.46	14.33	10.4	69.1	$\cdots$	$\cdots$	Y	Y
IGR J21277+5656	$\cdots$	13.27	13.21	13.08	13.27	9.18	40.9	$\cdots$	$\cdots$	Y	Y
IRAS 04124-0803	17.79	16.03	15.95	15.45	14.96	9.8	80.1	$\cdots$	$\cdots$	Y	Y
IRAS 05218-1212	16.44	15.45	14.71	14.22	14.20	10.46	50.5	$\cdots$	$\cdots$	Y	Y
IRAS 05589+2828	$\cdots$	15.36	14.87	13.81	13.42	10.41	81.6	$\cdots$	$\cdots$	Y	Y
KAZ 320	15.94	15.20	15.00	15.07	14.61	9.7	34.9	$\cdots$	$\cdots$	Y	Y
LEDA 138501	$\cdots$	18.17	19.56	18.16	18.35	8.59	99.0	$\cdots$	$\cdots$	Y	Y
MRK 1044	15.49	14.54	13.88	13.52	13.40	9.88	36.9	$\cdots$	$\cdots$	Y	Y
Mrk 290	18.37	15.74	15.19	14.86	14.71	9.8	52.9	$\cdots$	$\cdots$	Y	Y
Mrk 335	16.26	15.34	14.94	14.89	14.66	9.47	71.1	$\cdots$	$\cdots$	Y	Y
Mrk 509	14.91	14.21	13.77	13.60	13.26	10.39	56.4	$\cdots$	$\cdots$	Y	Y
Mrk 704	17.48	15.04	14.30	13.78	13.55	10.34	40.5	$\cdots$	$\cdots$	Y	Y
Mrk 841	16.55	16.06	15.45	15.00	15.02	9.97	82.4	$\cdots$	$\cdots$	Y	Y
RX J2044.0+2833	15.28	15.19	14.64	14.48	14.50	10.37	48.3	$\cdots$	$\cdots$	Y	Y
SDSS J104326.47+110524.2	19.16	17.31	17.33	16.80	17.30	8.65	70.4	$\cdots$	$\cdots$	Y	Y

[0] This table is also available in its entirety as a supplementary file in ASCII format.

[1] Measured host galaxy Petrosian mag after subtraction of AGN contamination using GALFIT. In some cases the galaxy was not detected in the u band.

[2] We used the software KCORRECT (Blanton & Roweis 2007) with the $ugriz$ photometry to calculate the stellar masses. This code uses the stellar population models of Bruzual & Charlot (2003) and photoionization models of Kewley et al. (2001).

[3] The value of the percentage of AGN to total (AGN and galaxy) light in the r band.

[4] Estimated reddening correction for dust based on AGN host $ugriz$ SED fitting using FAST (Kriek et al. 2009) with single-burst stellar population models.

[5] Estimated reddening correction for spiral galaxies based on inclination following Masters et al. (2010).

[6] We excluded the u photometry from this study because of the possibility of AGN contamination even after subtraction with GALFIT since $\%PS_r > 20$.

[7] We excluded the $griz$ photometry and determination of M_* from this study because of the possibility of AGN contamination even after subtraction with GALFIT.

Table 5
Summary of Color Comparison

log M$_*$	Type	N	Mean $(g-r)$	P(K-S)%[1]	Mean $(u-r)$	P(K-S)%
9.6 to 10	BAT	37	0.62±0.15		2.42±0.91	
	Inactive	23041	0.63±0.15	41	2.03±0.43	10
	SDSS AGN	455	0.72±0.10	<0.01	2.31±0.29	36
10 to 10.3	BAT	39	0.68±0.12		2.18±0.36	
	Inactive	7542	0.76±0.12	<0.01	2.40±0.38	<0.01
	SDSS AGN	743	0.76±0.09	<0.01	2.40±0.39	<0.01
10.3 to 10.6	BAT	39	0.69±0.13		2.26±0.57	
	Inactive	3108	0.81±0.12	<0.01	2.56±0.22	<0.01
	SDSS AGN	397	0.78±0.09	<0.01	2.48±0.28	<0.01
>10.6	BAT	39	0.70±0.14		2.23±0.67	
	Inactive	820	0.81±0.04	<0.01	2.78±0.20	<0.01
	SDSS AGN	148	0.83±0.07	<0.01	2.65±0.27	<0.01

[1] Probability percentage from a Kolmogorov-Smirnov (K-S) test that the BAT colors are from the same parent population.

Table 6 Summary of Morphological Properties

Galaxy	R$_P$ [1] ″	C [2] R_{90}/R_{50}	Class [3]	b/a [4]	Broad [5]
2MASX J00253292+6821442	. . . [6]	. . .	M	0.43	
2MASX J01064523+0638015	12.8	3.10	S	0.80	
2MASX J03534246+3714077	8.66	3.03	I	0.56	
2MASX J04440903+2813003	30.8	2.92	I	0.91	
2MASX J05054575-2351139	7.14	3.37	I	0.87	
2MASX J06411806+3249313	9.11	2.93	M	0.82	
2MASX J07595347+2323241	15.7	2.80	S	0.49	
2MASX J09112999+4528060	9.22	2.90	I	0.70	
2MASX J12005792+0648226	17.9	3.30	I	0.55	
2MASX J16174158+0607100	9.53	2.83	S	0.25	
2MFGC 02280	15.4	2.99	S	0.21	
ARK 347	11.2	3.26	I	0.60	
ARP 102B	12.1	3.55	E	0.79	
CGCG 102-048	10.5	3.04	S	0.36	
CGCG 300-062	14.0	2.73	S	0.77	
CGCG 312-012	8.52	3.04	E	0.95	
CGCG 420-015	13.7	3.27	E	0.77	
CGCG 427-028	14.6	2.58	I	0.22	
ESO 506-G027	44.9	3.74	S	0.31	
FAIRALL 272	18.6	3.21	M	0.61	
IC 0486	17.5	3.04	S	0.65	
IC 0751	16.9	2.85	S	0.28	
IC 2461	29.2	3.00	S	0.22	
IC 2515	16.6	3.42	S	0.22	
LEDA 170194	16.7	2.66	S	0.90	
LEDA 214543	10.6	3.13	I	0.87	
M106	216.	3.01	S	0.38	
MCG -01-05-047	66.1	2.87	S	0.13	
MCG -01-24-012	27.9	2.75	S	0.56	
MCG -01-40-001	39.6	2.65	S	0.34	
MCG -02-08-014	11.9	3.09	S	0.16	
MCG -02-12-050	24.1	2.88	M/S	0.89	
MCG -05-14-012	15.6	3.39	M/I	0.86	
MCG -05-23-016	15.4	3.26	I	0.45	
MCG +02-21-013	22.0	2.65	I	0.43	
MCG +04-48-002	20.8	2.73	M/S	0.36	
MCG +05-28-032	12.9	2.88	S	0.51	
MCG +06-24-008	17	2.44	S	0.26	
MCG +06-49-019	18.4	3.18	S	0.64	
MCG +11-11-032	11.8	3.02	S	0.45	
MCG+10-17-061	8.52	2.67	I	0.92	
Mrk 1210	15.6	2.93	E	0.86	
Mrk 18	8.5	3.15	I	0.15	
Mrk 198	7.71	3.31	S	0.86	
Mrk 268	12.8	3.31	I	0.45	
Mrk 348	55.0	3.19	S	0.97	
Mrk 417	9.1	3.18	E	0.77	

Continued on Next Page. . .

TABLE 6 – Continued

Galaxy	$\mathbf{R}_\mathrm{P}$ [1] $''$	C [2] R_{90}/R_{50}	Class [3]	b/a [4]	Broad [5]
Mrk 463E	12.6	2.24	M	0.41	
Mrk 477	6.19	2.56	M	0.71	
Mrk 732	16.5	3.17	I	0.87	
Mrk 78	$\cdots$	$\cdots$	I	0.61	
NGC 0835	24.3	2.99	M/S	0.45	
NGC 1012	47.8	2.57	S	0.51	
NGC 1052	44.0	3.06	E	0.56	
NGC 1142	28.0	2.87	M	0.48	
NGC 1194	35.8	3.22	I	0.47	
NGC 1275	52.1	3.02	M	0.74	
NGC 2110	53.9	3.35	E	0.74	
NGC 235A	11.5	3.09	M	0.52	
NGC 2992	41.4	3.09	M	0.30	
NGC 3079	119.	3.12	S	0.15	
NGC 3081	41.8	2.69	S	0.77	
NGC 3281	70.4	2.21	S	0.50	
NGC 3718	106.	2.65	S	0.42	
NGC 4102	51.8	2.60	S	0.41	
NGC 4388	81.7	3.13	S	0.18	
NGC 452	23.6	2.94	S	0.28	
NGC 4686	21.4	3.47	I	0.29	
NGC 4992	19.8	2.62	I	0.57	
NGC 5106	14.2	2.87	M/S	0.69	
NGC 513	13.9	2.27	M/S	0.51	
NGC 5231	26.0	2.44	S	0.51	
NGC 5252	25.1	3.20	I	0.56	
NGC 5290	53.4	2.86	S	0.27	
NGC 5506	56.2	2.30	I	0.23	
NGC 5610	26.5	2.32	S	0.33	
NGC 5728	82.3	2.58	S	0.57	
NGC 5899	57.0	2.60	S	0.43	
NGC 5995	21.1	3.43	I	0.32	
NGC 6240	36.5	2.95	M	0.51	
NGC 7319	$\cdots$	$\cdots$	M/S	0.55	
NGC 7682	37.1	2.78	S	0.89	
NGC 788	31.7	3.01	S	0.75	
NGC 973	$\cdots$	$\cdots$	S	0.14	
UGC 02724	40.8	1.87	S	0.65	
UGC 03995A	45.2	2.37	S	0.44	
UGC 05881	10.6	3.19	S	0.38	
UGC 06527 NED03	7	3.65	M/S	0.32	
UGC 07064	20.7	2.56	S	0.88	
UGC 08327 NED02	18.0	3.94	M/S	0.62	
UGC 11185 NED02	$\cdots$	$\cdots$	M/S	0.96	
UGC 12741	13.6	3.18	S	0.28	
2MASX J09043699+5536025	4.74	3.56	M	0.61	Y
2MASX J21355399+4728217	$\cdots$	$\cdots$	S	0.18	Y
ARP 151	4.94	3.15	M	0.16	Y
CGCG 031-072	10.5	3.04	I	0.59	Y
CGCG 046-033	11.3	2.50	S	0.75	Y
CGCG 122-055	12.9	2.97	I	0.75	Y
CGCG 198-020	20.6	2.45	I	0.71	Y
CGCG 319-007	12.2	2.68	I	0.61	Y
ESO 490-IG026	28.9	3.59	M	0.68	Y
ESO 511-G030	75.0	3.34	S	0.70	Y
IC 4329A	$\cdots$	$\cdots$	S	0.27	Y
KAZ 320	2.68	2.76	I	0.79	Y
KUG 1141+371	12.2	2.67	I	0.87	Y
KUG 1208+386	11.9	3.26	E	0.94	Y
MCG -01-13-025	16.8	3.19	E	0.61	Y
MCG -03-34-064	11.2	3.37	E	0.81	Y
MCG +01-57-016	7.12	3.78	S	0.86	Y
MCG +04-06-043	13.9	2.91	S	0.92	Y
MCG +04-22-042	15.2	2.92	S	0.56	Y
MCG +08-11-011	1.36	2.47	S	0.70	Y
Mrk 10	31.8	2.64	S	0.41	Y
Mrk 1018	11.1	3.72	M	0.52	Y
Mrk 110	4.64	3.68	M	0.62	Y
Mrk 1392	18.4	3.04	S	0.51	Y
Mrk 1469	8.82	3.26	I	0.35	Y
Mrk 279	19.0	2.73	M/S	0.58	Y
Mrk 352	$\cdots$	$\cdots$	I	0.83	Y
Mrk 464	2.6	3.23	I	0.76	Y
Mrk 50	8.03	2.94	E	0.60	Y
Mrk 520	15.0	3.63	S	0.62	Y
Mrk 590	29.3	2.92	M/S	0.97	Y

Continued on Next Page...

TABLE 6 – Continued

Galaxy	$\mathbf{R}_{P}$ [1] $''$	C [2] R_{90}/R_{50}	Class [3]	b/a [4]	Broad [5]
Mrk 595	7.2	3.24	M/E	0.62	Y
Mrk 705	5.14	3.50	I	0.88	Y
Mrk 728	7.08	3.08	E	0.64	Y
Mrk 739E	14.2	2.18	M/S	0.87	Y
Mrk 766	20.4	2.78	S	0.78	Y
Mrk 79	39.4	2.49	S	0.90	Y
Mrk 817	9.04	3.42	S	0.87	Y
Mrk 915	14.7	2.97	S	0.35	Y
Mrk 926	18.8	2.87	S	0.82	Y
NGC 2885	13.1	3	S	0.69	Y
NGC 3227	81	2.52	M/S	0.56	Y
NGC 3516	$\cdots$	$\cdots$	E	0.77	Y
NGC 3786	38.4	2.68	M/S	0.59	Y
NGC 4051	$\cdots$	$\cdots$	S	0.68	Y
NGC 4138	41.3	2.59	S	0.65	Y
NGC 4235	48.2	3.29	S	0.22	Y
NGC 4395	$\cdots$	$\cdots$	S	0.83	Y
NGC 4593	92.1	2.38	S	0.74	Y
NGC 5273	58.2	2.26	I	0.92	Y
NGC 5548	36.0	3.25	S	0.87	Y
NGC 5674	31.1	1.70	S	0.92	Y
NGC 5683	8.35	3.23	I	0.52	Y
NGC 5940	22.0	2.11	S	0.98	Y
NGC 6814	76.2	2.31	S	0.93	Y
NGC 7314	92.1	2.38	S	0.45	Y
NGC 7469	17.0	3.29	M/S	0.72	Y
NGC 7603	2.21	2.78	M/S	0.65	Y
NGC 7679	17.0	3.29	S	0.64	Y
NGC 931	48.6	3.45	M/S	0.21	Y
NGC 985	22.1	3.20	M	0.71	Y
SBS 1301+540	5.93	3.11	S	0.42	Y
UGC 03142	28.8	2.00	S	0.78	Y
UGC 03601	13.4	3.02	I	0.74	Y
UGC 12282	34.3	3.08	I	0.27	Y
UM 614	4.9	3.44	I	0.51	Y
VII Zw 073	7.36	2.58	S	0.91	Y

[0] This table is also available in its entirety as a supplementary file in ASCII format.

[1] The Petrosian radius was determined as the point when the Petrosian Ratio= $\int_{0.8r}^{1.25r} dr'\ 2\pi r'I(r')/\pi(1.25^2 - 0.8^2)r^2)/(\int_{0}^{r'} dr'\ 2\pi rI(r')/\pi r^2 = 0.2$.

[2] The concentration index is defined as the ratio of the radii containing 90 and 50 per cent of the Petrosian r-band galaxy light $C = R_{90}/R_{50}$.

[3] Galaxy Zoo Class where E stands for ellipticals, I, for intermediates, S, for spirals, and M for mergers/peculiars. For the Kitt Peak data, which has no Galaxy Zoo data, we use the Hubble Types from the RC3 with T = -6 to -4 corresponding to ellipticals, T = -3 to 0 to intermediates, T > 0 to spirals.

[4] We use the observed axial ratio (a/b) as a proxy for inclination.

An a/b=1 corresponds to a face-on galaxy. We use the g band and fit to the 25th mag arcsecond^{-2} isophote.

[5] Whether the galaxy has a broad-line AGN based on SDSS galaxy class or the available optical spectra. While we excluded these broad-line measurements from the morphological analysis, we have provided them for completeness. We subtracted the AGN model for these galaxies before determining the Petrosian radius and concentration index. However, the difficulty of perfectly subtracting the AGN light distribution makes these values more uncertain.

[6] The Petrosian radius and concentration failed to converge. This happened more often for close mergers or in a broad-line AGN where the AGN was imperfectly subtracted.